IEEE Access
Multidisciplinary | Rapid Review | Open Access Journal

IEEE RELIABILITY SOCIETY SECTION

Received 13 January 2024, accepted 5 February 2024, date of publication 12 February 2024, date of current version 12 March 2024.

Digital Object Identifier 10.1109/ACCESS.2024.3365143

RESEARCH ARTICLE

Variable Frequency Drives-Induced Torsional Stresses in Pumped Hydropower Storage Applications

PASCAL M. LINGOM, (Student Member, IEEE), JOSEPH SONG-MANGUELLE, (Senior Member, IEEE), SIMON PIERRE BETOKA-ONYAMA, (Student Member, IEEE), AND MAMADOU LAMINE DOUMBIA, (Member, IEEE)

Department of Electrical and Computer Engineering, University of Quebec at Trois-Rivières, Trois-Rivières, QC G8Z 4M3, Canada

Corresponding author: Joseph Song-Manguelle (joseph.song.manguelle@uqtr.ca)

ABSTRACT Despite consistent maintenance and monitoring equipment installed in pumped storage hydropower (PSH) facilities, many shafts and electrical component failures are reported, possibly resulting from undetected sources. These sources include undetectable vibrations or, in certain conditions, high-frequency mechanical or electrical harmonics. This paper presents a direct method for plotting Campbell diagrams of large motors supplied by variable frequency drives (VFDs) for torsional analysis purposes in PSH systems. These diagrams display the precise locations where torsional stress components induced by VFDs can interfere with shaft resonance modes. The method simplifies the determination of the magnitude of stimulus forces in the motor airgap that may threaten the shaft. The method has been successfully applied to two-level, three-level neutral-point clamped, and seven-level cascaded H-bridge multilevel inverters, which are commonly used industrially available VFD topologies for pumped PSH plants. The paper also discusses the theoretical motor-pump voltage, current, and torque spectra when driven by a cascaded H-bridge multilevel converter operating with bypassed and faulty cells. The accuracy of the theoretical developments is supported by selected simulations results at different operating points and different fault conditions. Hybrid experimental-numerical VFD-induced harmonic stress analysis is also performed to demonstrate the relevance of the proposed study.

INDEX TERMS Airgap torque, hydropower, pulse-width modulation, resonance, torsional analysis, torsional stress.

I. INTRODUCTION

A. BACKGROUND

HYdropower plants and pumped storage hydropower (PSH) facilities can offer significant services to the grid. With their ability to offer bulk energy storage and balance the grid, these facilities play a vital role in ensuring a reliable electricity supply [1]. They can enable frequency control with large inertia and power reserves to improve grid flexibility and resilience. An example of a single-line diagram of a reversible hydropower storage plant is shown in Figure 1. In one operation mode, the electricity is utilized to pump water from a lower reservoir to an upper reservoir when all the energy produced cannot be consumed [2], [3]. In such system configuration, the motor-pump controls the water flow. When needed, the stored potential energy of water is converted into a kinetic energy to drive the hydro-turbine which generates the electricity to be injected to the grid [2].

Despite monitoring equipment and regular maintenance, shaft element failures in pumped storage hydropower systems are still being reported in the literature. These failures are often caused by undetected sources, which can significantly impact the overall system performances [4], [5], [6], [7], [8]. The sources include undetectable vibrations and mechanical or electrical harmonics. They may induce premature material fatigue and ageing, leading to accelerated wear, tear, and

The associate editor coordinating the review of this manuscript and approving it for publication was Yu Liu.

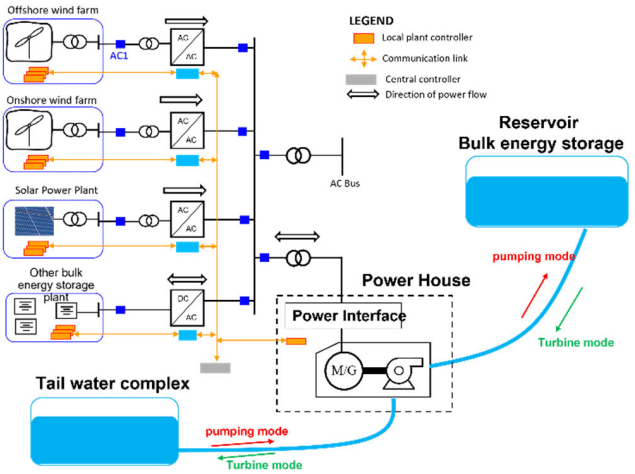

FIGURE 1. A single-line diagram of a pumped storage hydropower plant.

premature system failure [5], [9]. When a variable frequency drive (VFD) is used, risks of low-order vibrations increase. The VFD-induced vibrations may interfere with the natural frequencies of subsystems, leading to an increase in drivetrain torsional strain [10], [11], [12].

The Campbell diagram is a commonly used tool to show the interference points between the machine's airgap torque and shaft's natural frequencies [13]. These locations are those where torsional stresses may increase to threaten the shaft components. These Campbell diagrams depend on the VFD topology [14], [15]. The industry does not have a clear method explaining how to plot Campbell diagrams resulting from VFDs. This paper covers this gap in the practicing engineering community for VFD topologies commercially available and commonly used in PSH applications.

B. MOTIVATIONS AND BENEFITS

Engineers in charge of designing powered dams and PSH facilities must have a tool for performing accurate torsional analysis and stress evaluation of the rotating shafts. International standards require such analysis to ensure the integrity of the rotating shaft in its entire operating range [16], [17], [18]. Also, operational engineers developing predictive maintenance tools to the extend lifetime of these plants need an instrument that can provide vital information on critical shaft elements [19]. They also need a tool for conducting accurate root cause failure analysis shall a shaft element fail [20]. Finally, research and development engineers conducting the development of digital tools for replicating static and dynamic behaviors of PSH plants, such as digital twins, may need to include in their models the dynamics of the shaft, the generator, the VFD, and its controls, as well as the transformer and the transmission line [21]. Such tools may need to include the reversible energy flow from renewable sources to grid-scale storage and the impact of both grid contingencies and water-induced fluctuation on their models [22], [23].

C. IMPORTANCE OF THIS INVESTIGATION

This paper focuses on developing time-domain models of torsional stresses subjected to shaft elements, as illustrated in figure 2. First, the critical shaft components should be identified, such as bearings, rings, gear, turbine blades, and generators. Then design data and operational parameters are required. They include the type of AC machine, the type of VFD and its modulation parameters (carrier and operating frequencies), shaft materials and their strength, and transmission line and transformer impedance. They can be gathered from different sources, including PSH operators, equipment manufacturers, and open sources. The paper provides both time- and frequency-domain analytical expressions of torsional stresses generated by the VFDs. It also considers other sources of torsional stresses, such as water flow and internally generated mechanical-induced stresses possibly resulting from the failure of the shaft's elements. The results can be utilized to evaluate component degradation models. They can also be integrated into existing or digital twins under development, clearly predicting equipment lifetime [24]. Furthermore, tools such as electronic vibration suppression technology (e-VST) systems can utilize the results of this investigation to reduce the torsional stresses of the shaft's elements.

D. CONTRIBUTIONS

The main contributions provided in this paper are:

i A general analytical expression of the torsional stresses created by electromagnetic airgap torque of AC machines used in PSH applications.
ii Direct methods to plot Campbell diagrams resulting from pulse-width-modulated (PMW) voltage source inverter (VSI) systems, regardless of the power part architectures (two and multilevel arrangements), considering the PWM carrier frequency.
iii A direct method to plot a Campbell diagram resulting from any configuration of parallel connection of VSI modules with synchronized or interleaved PWM commands.
iv A theoretical analysis of harmonics in the cascaded H-bridge VSI system with faulty cells is proposed.

Finally, offline and real-time simulations are performed, and results are analyzed for a 35 MVA VSI system to demonstrate the accuracy of the method. Parallel connection of two-level inverters, three-level neutral-point-clamped (NPC) converters, and cascaded H-bridges multilevel inverters with synchronized and interleaved PWM commands were simulated and discussed in this paper.

The paper is organized as follows: Section II discusses the aging of shaft elements resulting from torsional stresses from a list of possible stimulus forces induced by oscillating vibrating components; their mathematical formulation is provided, as well as a high-level dynamic model of such systems such as the shafts, the VFD and its controls, transmission cable, and transformer. Section III provides a generic formulation of torsional stresses induced by VFDs based on the electric

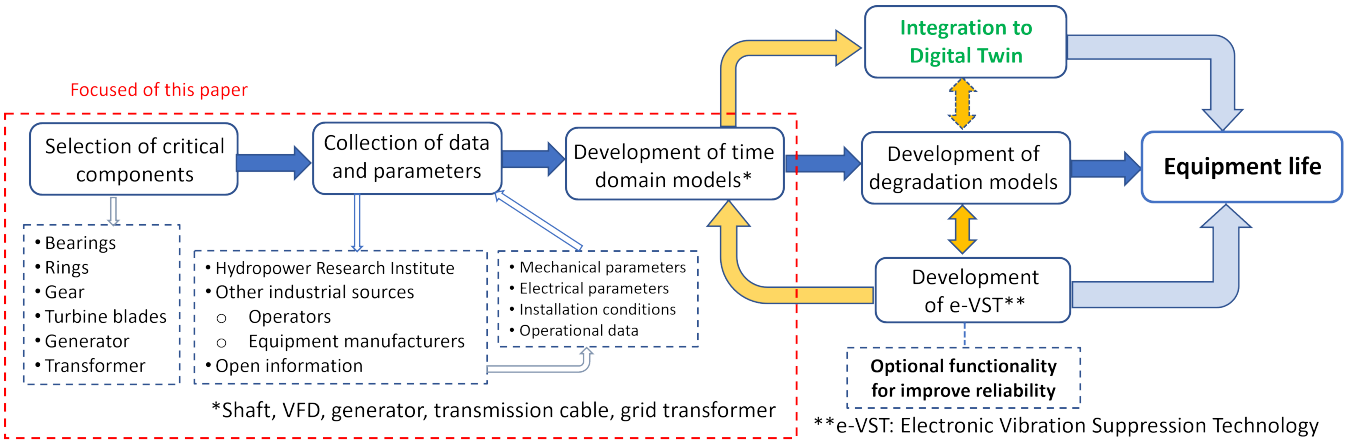

FIGURE 2. Flowchart to develop equipment life estimation of PSH mechanical components.

harmonics they are generating. Specific arrangements of VFD topologies suitable for PSH applications are discussed in Section IV. Section V is dedicated to discussing the operations of PSH systems in the event of power module failure. Section VI derives and discusses the instantaneous expressions of the torsional stresses generated by a specific VFDs.

The proposed mathematical expressions are validated through numerical simulations, and selected results are discussed in Section VII.

II. TORQUE COMPONENTS ON A PSH SHAFT SYSTEM

A. AGEING OF SHAFT ELEMENTS FROM TORSIONAL STRESSES

An element aging is an occurrence of irreversible changes in its material, affecting its ability to perform the required service [25]. Causes of aging are factors imposed by operation, environment, technology, or test that influence the performance of the component subjected to stresses [26]. The dependence of aging A on the property p, can be written as:

$$A = F(p) \tag{1}$$

where $p = P/P_0$ is the observed property P, with respect to the unaged property P_0. Aging A is a dimensionless quantity. Failure occurs when p reaches a limit value p_L. The process of fatigue failure is divided into two parts: the formation of the fatigue fissure itself and the growth of the fissure. It is understood that at the start of the process, $A = 0$ (no crack), and at the end, when the crack appears, $A = 1$ (apparition of irreversible change) [27], [28]. The aging rate is:

$$R = \frac{dA}{dt} \tag{2}$$

R is assumed to depend only on stresses applied to the element, and not on time t, which is the monotonic time variation of P. Also, the machine element is subjected to a stress of magnitude S_j $(j = 1 \ldots N)$ a certain number of times per unit of operation. The unit of operation can be chosen as a revolution per second. It is possible to predict how long an element, subjected to a cyclic stress can operate before a crack occurs. Usually, the *S-N* curves or the "Woehler curves" are used for this purpose. It represents a plot of the relationship between the cyclic stress level against the number of cycles to material failure [29]. A failure can occur even if the stress is less than the yield strength (endurance limit) of the material. The effective stress applied to an element is usually a combination of both a mean stress and an oscillating component with a constant magnitude. The mean shear stress does not influence the fatigue life of a ductile structural component subjected to a cyclic load [29], [30]. In real life, the frequency of the stress cycles can become a factor if it is near the natural frequency of the shaft. In that case, its magnitude increases proportionally to time until it reaches a final value that depends on the damping coefficients.

B. POSSIBLE SOURCES OF VIBRATION IN PSH SHAFTS

There are three possible sources of vibrations in PSH shafts that are discussed in this section: hydraulic-induced, mechanical-induced, and electrical-induced vibrations [5].

1) HYDRAULIC-INDUCED VIBRATIONS

From the electrical machine point of view, these vibrations may be seen as process or load-induced vibration components. They may result from the hydro-dynamic of the high-pressure water propagating through the upper or lower penstock pipes and water moved by the turbine blades [31].

2) MECHANICAL-INDUCED VIBRATIONS

Mechanical vibrations are those resulting from the mechanical elements of the shaft. They may be generated from structural irregularities, inadequate lubrication, destruction of turbine or pump blades, and destruction of gear teeth [32]. They may also result from physical installation conditions of the system, such as frame vibration resulting from poor mechanical connections of the machine frame, physical

vibrations of the casing where the machine is tightened to the building (e.g., micro-seismic vibrations resulting from other equipment) [33], [34].

3) ELECTRICAL-INDUCED VIBRATIONS

When an AC motor is introduced in a rotating shaft system, new stimulus forces are created in the form of electromagnetic airgap torque [35]. Furthermore, when the motor is supplied by a VFD for an adjustable speed operation, the airgap torque is theoretically having an infinite number of periodic components, due to distorted voltages and currents [36]. The torque components are oscillatory with dynamic frequencies and magnitudes. The machine' design also produces oscillating torque (cogging, commutation, and reluctant) [37].

C. FORMULATION OF NON-ELECTRICAL-INDUCED TORQUE

The shaft stress formulated in the form of electromagnetic torque, $t_e\,(t)$, generated in the machine's airgap can be grouped into two main categories as mathematically formulated in (3):

i Non-electrical-induced components, $t_{NE}\,(t)$, which result both from mechanical and hydraulic vibrations.
ii Electrical-induced components, $t_E\,(t)$, which are generated from the voltage supply (e.g., VFD).

$$t_e(t) = t_{NE}(t) + t_E(t) \tag{3}$$

All k-hydraulic and mechanical induced torque components are converted to a set of average quantities (4a), superposed to periodic components with different magnitudes and frequencies (4b).

The frequencies that are multiples of their original frequency ω_{NE_k}. All q-mechanical components (4c) have their frequencies proportional to the rotational speed ω_0 of a $P-$ pole motor.

$$t_{NE}(t) = \sum_{i=1}^{\infty} T_{NE_{DC},i} \tag{4a}$$

$$+ \sum_{k=1}^{\infty}\sum_{j=1}^{\infty} T_{NE,k,j}\cos\left(k.\omega_{NE_{k,j}}t + \theta_{NE_k}\right) \tag{4b}$$

$$+ \sum_{q=1}^{\infty} T_{mec,q}\cos\left(q.P.\omega_0.t + \theta_{mec,q}\right) \tag{4c}$$

D. FORMULATION OF ELECTRICAL-INDUCED TORQUE

As expressed in (5), there are two sets of electrical-induced torque components, $t_{e(t)}$, in the machine's airgap: construction-induced, $t_{eCons}\,(t)$, and power supply-induced, $t_{eVFD(t)}$:

$$t_e(t) = t_{eCons}(t) + t_{eVFD}(t) \tag{5}$$

1) CONSTRUCTION-INDUCED TORQUE COMPONENTS

They result from the imperfection of the machine design and construction (airgap eccentricity, slots of the stator and rotor, manufacturing, and assembly tolerances, etc.). They include cogging, reluctance, and commutation torques, and are proportional to the rotational speed of the machine [14]. They are lumped in (4c) and shown in (6).

$$t_{eCons}(t) = \sum_{q=1}^{\infty} T_{mec,q}\cos\left(q.P.\omega_0 t + \theta_{mec,q}\right) \tag{6}$$

2) POWER SUPPLY INDUCED TORQUE COMPONENTS

These are torque components created in the machine's airgap because of the electric power supplying the machine and they are discussed in Section IV.

III. INTEGRATED SYSTEM MODEL FOR TORQUE ANALYSIS

A. TRANSMISSION LINE AND TRANSFORMER MODELS

The transmission line is modeled as a multiple pi-section system. It can also be modeled as a two-terminal system with passive components with distributed parameters, R_C, L_C, and C_c [38]. In that case, the cable sending- and receiving-end voltages and currents are related according to (7).

$$\begin{bmatrix} v_{SE} \\ i_{SE} \end{bmatrix} = \begin{bmatrix} \cosh(\lambda d) & -z_w\sinh(\lambda d) \\ Y_w\sinh(\lambda d) & -\cosh(\lambda d) \end{bmatrix} \cdot \begin{bmatrix} v_{RE} \\ i_{RE} \end{bmatrix} \tag{7}$$

where the propagation constant of the transmission line over a distance d is given by (8a), the cable impedance Z_c is given by (8b); the respective inductive reactance, and capacitive admittance of the cable are (8c) and (8d)

$$\lambda = \sqrt{L_c C_c} \tag{8a}$$

$$Z_c = R_c + jX_c \tag{8b}$$

$$Y_c = j\omega C_C \tag{8c}$$

$$Z_W = \sqrt{Z_c/Y_C};\; Y_W = 1/Z_W \tag{8d}$$

Frequency-dependent resistances r_c of the cable to replicate the skin effect can be inserted in the capacitor branches. The grid side and the VFD side transformers are modeled as a resistance series connected to an inductance, and they are lumped with the cable impedance, but they can be neglected due to the length of the transmission cable.

B. SHAFT MODEL

A dynamic shaft model can be established using the lumped parameters of the elements, such as their mass moments of inertia, damping coefficients, and stiffness constants derived from Newton's second law shown in (9) [39], [40].

$$j\frac{d\theta^2}{dt^2} + D\frac{d\theta}{dt} + K\theta = T_{ext} \tag{9}$$

where J, D, and K are, respectively, the matrixes of moments of inertia, damping coefficients, and stiffness constants. The dynamic equation (9) should be solved with the forced excitations given in the matrix of externally applied forces shown in (8). It contains the airgap electromagnetic torque stresses, T_M(t), and the water-flow torque stress, $T_1(t)$. All

other components are zeros when there is no failure on the shaft and non-zero when a failure occurs at the j^{th} node:

$$T_{ext} = \left[T_1, 0, \ldots, T_j, 0, \ldots, T_M\right]^T \tag{10}$$

C. VFD SWITCHING MODEL

The cable receiving-end voltage usually supplies the VFD input rectifier, generating a DC-link voltage with an average value of $V_{DC} = 1.35V_{SE}$. For the sake of simplicity, it is assumed that the DC-link capacitor is large enough to decouple the dynamics of the grid and motor sides. The VFD is modeled by its PWM generation unit. This unit generates a switching function that is multiplied by the DC-link voltage [40]. Regardless of the operation mode of the machine, voltage, and current quantities can be written in the generic forms in a steady state, as shown in (11) and (12) [41]:

$$v_a(t) = \sum_{m_v=0}^{\infty}\sum_{n_v=0}^{\infty} V_{m_v,n_v}\cos\left(m_v\omega_k t \pm n_v\omega_0 t + \theta^v_{m_v,n_v}\right) \tag{11}$$

$$i_a(t) = \sum_{m_i=0}^{\infty}\sum_{n_i=0}^{\infty} I_{m_i,n_i}\cos\left(m_i\omega_k t \pm n_i\omega_0 t + \theta^i_{m_i,n_i}\right) \tag{12}$$

where ω_k is an arbitrary frequency (for example the PWM carrier frequency) and ω_0 the fundamental frequency; (m_v, n_v) and (m_i, n_i) are arbitrary integer sets; $V_{m_v n_v}$ and $I_{m_i n_i}$ are the magnitudes of voltage and current. For a three-phase voltage system, $v_a(t)$ is the reference phase voltage. Therefore, voltages and currents on the two other phases are respectively phase shifted by $n_v = 2\pi/3$ and $n_v = 4\pi/3$.

The arbitrary integer sets (m_v, n_v) and (m_i, n_i) depend on the inverter topology and its modulation strategy.

D. MOTOR AIRGAP MODEL

The motor airgap creates the power supply-induced torque components from the voltage supplied to the machine and the current requested by the machine to generate the needed torque in motoring mode. And they result from a combination of the back-electromagnetic forces (generator mode) created by the machine and the current flowing to its electrical load. The torque is calculated by (13). The principle of transforming the machine's voltages (11) and currents (12) is described in [40]. The integrated model of the PSH shaft system for the evaluation of torsional stresses is shown in figure 3.

The interaction of voltage and current components in the motor's airgap creates infinite electromagnetic torque harmonic components. The machine instantaneous airgap torque induced by the power supply is analyzed in the stationary and orthogonal $\alpha\beta$-coordinates for harmonic evaluation. It offers the advantage of analyzing the torque waveform as a complex quantity without cumbersome mathematical developments, while accurately tracking all relevant harmonics. The rotating dq-coordinates would require an infinite synchronization to all harmonic frequencies as well as complicated reverse transformations of the results back to the frequency domain. By replacing (11) and (12) in (13), the theoretical lines of the Campbell diagram are given in (14). The torque magnitudes and phase are given in (15) and 16). The torque equations are given in (17), as shown at the bottom of the next page. Where ε_{n_v} and ε_{n_i} are $\in (-1, 1)$. Only a few of the components in (17) are pertinent for a torsional analysis. In PWM VSI systems, the arbitrary frequency is the carrier frequency: $\omega_k = \omega_c$, which is usually in the range of 1.0 kHz or more. Certain combinations of (m_v, n_v) induce cancellation of voltage harmonics.

$$t_{eVFD}(t) = \frac{3}{2}\frac{P}{2}\left(\psi_\alpha(t).i_\beta(t) - \psi_\beta(t).i_\alpha(t)\right) \tag{13}$$

$$\omega_h = \left(m_i - \frac{\varepsilon_{n_i}}{\varepsilon_{n_v}}m_v\right)\omega_k \pm \left(n_i - \frac{\varepsilon_{n_i}}{\varepsilon_{n_v}}n_v\right)\omega_0 \tag{14}$$

$$T_{eh} = \varepsilon_{n_v}.\frac{3}{2}\frac{P}{2}\frac{V_{m_v,n_v}}{m_v\omega_k \pm n_v\omega_0}I_{m_i,n_i} \tag{15}$$

$$\theta_h = \theta^i_{m_i,n_i} \pm \frac{\varepsilon_{ni}}{\varepsilon_{nv}}\theta^v_{m_v,n_v} \tag{16}$$

Furthermore, depending on the VFD topology and its modulation strategies, certain combinations of (m_v, n_v) lead to the cancellation of certain voltage and current harmonics. The modulation strategy is therefore critical in ensuring that unwanted torque harmonics are cancelled, or their magnitudes are substantially low to threaten the endurance limits of shaft elements. The following section discusses the VFD topologies, and their modulation strategies utilized in PSH applications aiming to evaluate the torque stress they produce.

IV. VFD TOPOLOGIES FOR PSH PLANTS

A. GENERAL ARRANGEMENTS

The three types of system arrangements utilized in PSH applications are summarized in figure 4 with their respective power ranges [42], [43], [44]. Layout 1, figure 4a, is used when the plant capacity is below 25 MW. Layout 2, figure 4b is for PSH plants below 100 MW. These two topologies use synchronous machines, whereas Layout 3, figure 4c, uses a doubly-fed induction machine. In such a system configuration, about 30% of the total power flows through the rotor, which enables a very high-output power production for the plant, usually 100–250 MW [43]. This paper is limited to VFD topologies suitable for Layout 2 only, as they are the ones suitable for the US applications [4].

B. INVESTIGATED VFD TOPOLOGIES

There are numerous VFD topologies that can be utilized for Layout 2. Figure 5 shows two main high-level configurations with their respective power ranges. A three-phase machine supplied by a set of parallel connected identical power converters coupled through coupling; in this case, it is a twelve-phase synchronous machine supplied by identical power converters [figure 5b]. In this case, the airgap torque is the sum of all individual torque generated by the converter supplying each three-phase stator windings [41].

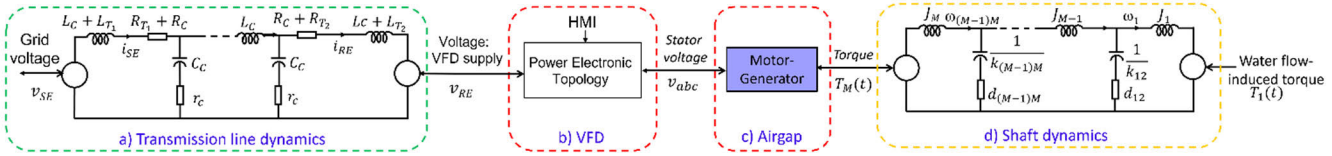

FIGURE 3. An integrated electromechanical model of a PSH plant.

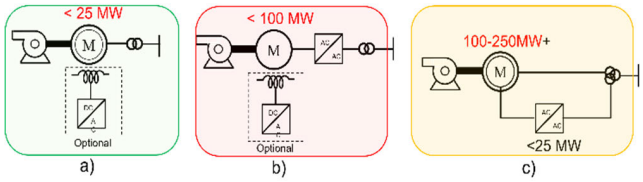

FIGURE 4. High-level Power system arrangements of PSH plant [3].

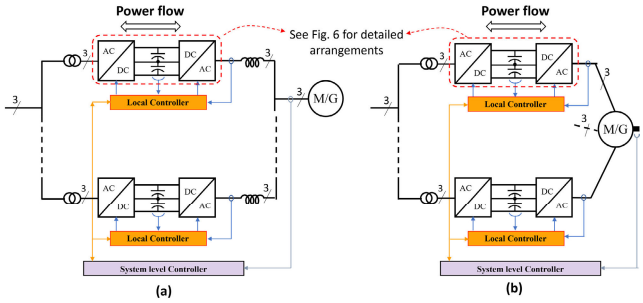

FIGURE 5. High-level system configurations of VFDs for PSH applications.

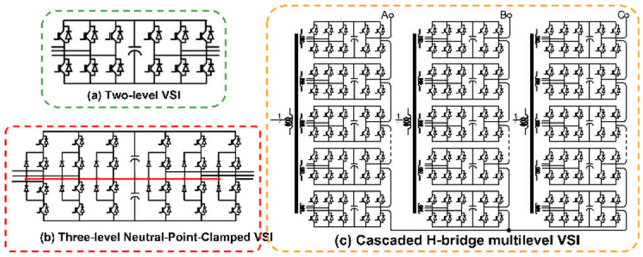

FIGURE 6. Detailed arrangements of VFDs for PSH applications up to 100 MW.

The investigated families of back-to-back power converter topologies are shown in figure 6. They include: 1) A two-level VSI topology, suitable for PSH applications up to 25MW); 2) A three-level NPC VSI suitable for power exceeding 30 MW, and the cascaded H-bridge multilevel VSI, for power exceeding 60 MW [42], [43], [44].

C. EFFECTS OF INTERVEALED PWM COMMANDS

Parallel connection of VFD uses coupling inductors, which convert VFD voltages to currents, which are added at the coupling point before flowing to the motor stator. The PWM commands can be synchronized or interleaved [44], [45]. Synchronized commands enable the system to behave like a large single VFD. Interleaved commands are phase-shifted by a pre-calculated angle. Let us assume there are k paralleled VSIs. Each converter $j \in \mathbb{K} = \{1, \ldots, k\}$ generates a phase voltage $v_{a,j}(t)$. A regular asymmetric sampling PWM is utilized. The voltages are generated by comparing a sinewave with a frequency ω_0 to a triangle signal with a frequency ω_c. The triangle signal is phase shifted by $\theta_{c,j}$ with respect to the phase a reference sinewave.

$$\theta_{c,j} = (j-1)\frac{\pi}{k}, j \in \mathbb{K} \tag{18}$$

Each voltage harmonic of the j^{th} converter for a set of (m_v, n_v) has a magnitude $V_{m_v n_v, j}$. Thus, $v_{a,j}(t)$ is given in (19):

Let's assume the coupling inductors have the same impedance. All DC-link voltages are equal. When paralleled, the only dominant current harmonics produced by the VFDs are the baseband and common-mode components with a rank multiple of $k(2m_i)$.

$$v_{a,j}(t) = \sum_{m_v=0}^{\infty}\sum_{n_v=0}^{\infty} V_{m_v,n_v,j}\cos\left(x_{m_v,n_v,j}(t) + m_v\theta_{c,j}\right) \tag{19a}$$

$$x_{m_v,n_v,j}(t) = m_v\omega_k t \pm n_v\omega_0 t + \theta^v_{m_v,n_v} + \delta_{m_v,n_v} \tag{19b}$$

All components at $k(2m_i) \pm 1$ for all applicable n_i are canceled. All other harmonic components are reduced. Consequently, the resulting torsional stress will see a cancellation or drastic reduction on its corresponding harmonics [14], [41].

$$t_{eVFD}(t) = \sum_{m_v=0}^{\infty}\sum_{n_v=0}^{\infty}\sum_{m_i=0}^{\infty}\sum_{n_i=0}^{\infty}\left[\varepsilon_{n_v} * \frac{3P}{2}\frac{V_{m_v,n_v}I_{m_v,n_v}}{m_v\omega_k + n_v\omega_0}\right]\cos\left(\left(\left(m_i - \frac{\varepsilon_{n_i}}{\varepsilon_{n_v}}m_v\right)\omega_k \pm \left(n_i - \frac{\varepsilon_{n_i}}{\varepsilon_{n_v}}n_v\right)\omega_0\right)t + \left(\theta^i_{m_i,n_i} - \frac{\varepsilon_{n_i}}{\varepsilon_{n_v}}\theta^v_{m_v,n_v}\right)\right) \tag{17}$$

D. EFFECTS OF PWM COMMANDS TO A MULTI-PHASE MACHINE

Let us assume the AC machine has k sets of three-phase windings supplied by k PWM-VSIs, each converter $j \in K = \{1, \ldots, k\}$ generates a phase voltage $v_{a,j}(t)$. The electrical phase-shift angle between consecutive winding sets is (20a), [44]. The flux formed in the airgap is equivalent to the one produced by the k sets of voltages, with a phase shift shown in (20b). In that case, the voltage harmonic families are given in (21).

$$\theta_{e,j} = \frac{\pi}{3k}, \tag{20a}$$

$$\theta_{0,j} = (j-1)\frac{\pi}{3k},\ j \in \mathbb{K} \tag{20b}$$

$$v_{a,j}(t) = \sum_{m_v=0}^{\infty}\sum_{n_v=0}^{\infty} V_{m_v,n_v,j}\cos\left(y_{m_v,n_v,j}(t) + n_v\theta_{0,j}\right) \tag{21a}$$

$$y_{m_v,n_v,j}(t) = m_v\omega_k t \pm n_v\omega_0 t + \theta^{v}_{m_v,n_v} + \delta_{m_v,n_v} \tag{21b}$$

The sum of the voltages induces a cancellation of all harmonic components formed when n_v is an odd multiple of $3k$.

$$n_v = 3k(2l+1);\ l \in \mathbb{N} \tag{22}$$

Moreover, only components with frequencies even multiple of $3k$ will have their magnitude multiplied by k.

$$n_v = 3k(2l);\ l \in \mathbb{N}^* \tag{23}$$

All other harmonics will have their magnitudes smaller than k-times the magnitude of their individual harmonics, which will reduce their torsional stresses.

V. PSH SYSTEMS OPERATION WITH FAILED CELLS

A. ROBUSTNESS AND FAILED MODE RECONFIGURATIONS

1) SYSTEM CONFIGURATION WITH FAILED TWO-LEVEL OR THREE-LEVEL NPC CONVERTERS

So far, the analysis assumes all power modules are operating in normal mode. However, in case of a failure, the location of the torsional stresses in the frequency domain can significantly change, depending on how the faults are handled. For example, if k-power modules are parallel connected, then a failure of ϵ- power modules which are subsequently disconnected from the operating system, will induce a shift of harmonics to be identical to the one from a $(k-\epsilon)$-power module system. To interleave the PWM commands, the phase-shift-angle given in (18) shall be adjusted to $\theta_{c_{new},j}$:

$$\theta_{cnew,j} = (j-1)\frac{\pi}{k-\varepsilon},\quad j \in \{1, \ldots, k-\epsilon\};\ \varepsilon < k \tag{24}$$

Figure 7 shows a system configuration with a failed and disconnected power module (for two-level and three-level NPC converters). The system level controller is responsible for the power part reconfiguration (i.e., order

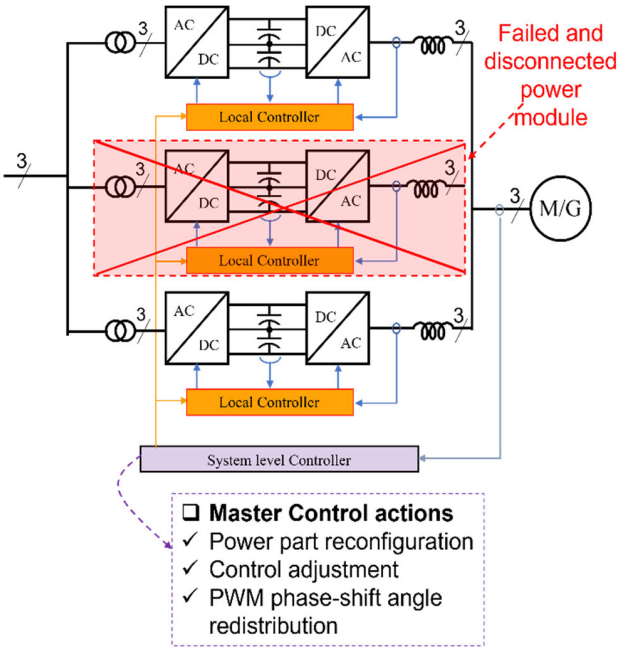

FIGURE 7. System configuration with failed power module.

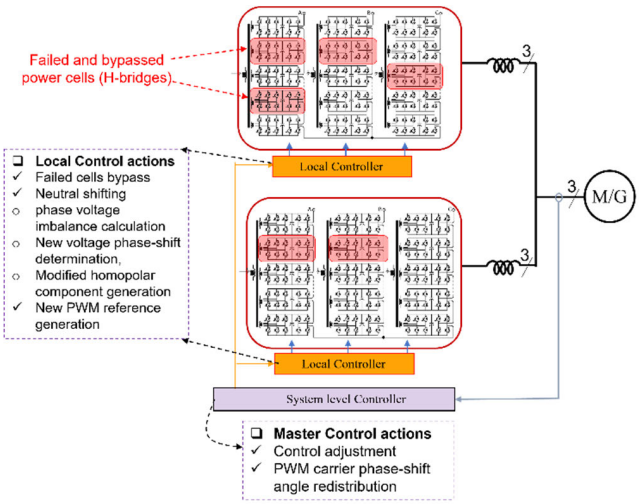

FIGURE 8. System configuration with partially failed power modules but with failed and bypassed H-bridge cells.

disconnection of failed the power module), adjustment of power module control parameters (e.g., reduced power generation), and calculation of new PWM phase-shift angles to interleave the PWM commands. Theoretically, for a given PWM strategy, all PWM-VSIs generate voltage harmonics located at identical frequencies; only their magnitudes differ from one VSI topology to another, particularly when PWM commands are synchronized. Therefore, if a power module fails and is disconnected from the operating system, only the magnitude of the torsional stress will slightly increase. These statements are only valid for the two-level and the three-level NPC regenerative inverters.

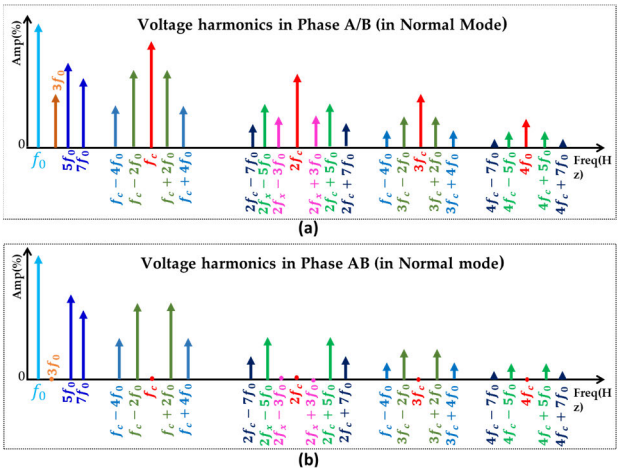

FIGURE 9. Harmonic analylis in Balanced conditions: Voltage harmonic in phase A; (b): Voltage harmonic in phase AB.

2) SYSTEM CONFIGURATION BASED ON CHB-VSI WITH FAILED CELLS

The fault management of the cascaded H-bridge regenerative converter topology enables higher system availability than the other system architectures. Because of an increased number of power cells (H-bridges), there is no need to disconnect a complete power module in case of abnormal operation.

The system can operate with failed H-bridge cells, where the PWM commands of a given three-phase system are adjusted through a neutral-shift method such that the VFD produces unbalanced line-to-neutral voltages. In contrast, the line-to-line voltages remain balanced, [46], [47], [48], [49]. Figure 8 shows the system configuration with partially failed power modules but with completely bypassed H-bridge cells. The local controllers order any failed cell to be ignored by closing the output circuit breaker and disconnecting it from the system by opening the module input circuit breaker. Circuit breakers are not shown for the sake of simplicity. Once the power stage is reconfigured, the phase voltage imbalance is calculated, new voltage phase-shift angles are determined, the new homopolar component is computed, and the new PWM references are generated to ensure that balanced line-to-line voltages are generated at the output of the unhealthy power module [46], [47], [48], [49]. Finally, the master controller adjusts the current references that each power module should generate and calculates the new carrier phase-shift angles for each power module if needed.

B. HARMONIC ANALYSIS IN CHB-VSI SYSTEM WITH FAULTY CELLS

Let's consider a CHB PWM-VSI system with k_i-series connected H-bridge power cells in the phase i, of a three-phase system. Each cell is supplied by a dc voltage $v_{dc,ij} = v_{dc}$; such that $v_{dc} = 1$ for healthy cells and $v_{dc} = 0$ for failed cells. In balanced conditions, the phase-shift between phase voltages is: $\theta_{0,i} = (i-1)\frac{2\pi}{3}, i \in \mathbb{K} = \{a = 1, b = 2, c = 3\}$. In that case, the total perceived DC-link voltage per phase is given by:

$$V_{dc,i} = k_i v_{dc} \tag{25}$$

Consequently, in normal mode operation when all k_i-power modules are operational on phase i, the reference voltage with a frequency fundamental ω_0 can be written as:

$$v_i^*(t) = m_i V_{dc} \sin\left(\omega_0 t - \theta_{0,i}\right) \tag{26}$$

where $m_i \in [0, 1]$ is the PWM modulation index applied to phase i. The maximum achievable phase voltage resulting from the modulator in normal mode is given by:

$$\max_{i\in P}\left(v_i(t)\right) = v_i(x^*) = V_{max,i}, \forall x^* \in \arg\max_{i\in P} v_i(t) \tag{27a}$$

$$V_{max,i} = \frac{\sqrt{3}}{2} V_{dc,i} \tag{27b}$$

Let's assume there are ϵ_i failed H-bridge cells on phase i, such that $\epsilon_i < k_i$. In that case, the perceived maximum voltage in the affected inverter phase is given in (28).

$$V_{max,i}^F = (k_i - \epsilon_i)\frac{\sqrt{3}}{2} v_{dc} \tag{28}$$

When voltages at the motor terminals are unbalanced, it leads to unequal power distribution across the motor phases. This imbalance causes higher current flow in the phase with higher voltage, resulting in several issues, such as high current imbalance, pulsating torque, and mechanical Stresses. As a result, evaluating VFD-induced torsional stresses under unbalanced conditions (without and with the neutral-shift approach) is critical for the completeness of the design because the locations of harmonics are unknown.

1) HARMONIC ANALYSIS IN NORMAL MODE

In normal (ideal) operating mode for both linear and overmodulation regions, the analytical expression of the CHB-VSI LN-voltage $v_i^N(t)$ can be written as follows:

$$v_i^N(t) = k * V_{0,1} \cos\left[\omega_0 t - (i-1)\frac{2\pi}{3}\right] \tag{29a}$$

$$+ k \sum_{n_v=2}^{\infty} V_{0,2n_v-1} \cos\left[(2n_v - 1)\left(\omega_0 t - (i-1)\frac{2\pi}{3}\right)\right] \tag{29b}$$

$$+ k \sum_{m_v=1}^{\infty} V_{(2m_v-1),0} \cos\left((2m_v - 1)(\omega_c t - \theta_c)\right) \tag{29c}$$

$$+ \sum_{m_v=1}^{\infty} \sum_{\substack{n_v=-\infty \\ n_v \neq 0}}^{\infty} V_{(2m_v-1),2n_v} \cos\left[\begin{matrix}(2m_v - 1)(\omega_c t - \theta_c) + \\ 2n_v\left(\omega_0 t - (i-1)\frac{2\pi}{3}\right)\end{matrix}\right] \tag{29d}$$

$$+ \sum_{m_v=1}^{\infty} \sum_{n_v=-\infty}^{\infty} V_{2m_v,2n_v+1}$$

$$\cos\left[\begin{array}{c} 2m_v\left(\omega_c t-\theta_c\right)+ \\ \left(2n_v+1\right)\left(\omega_0 t-(i-1)\dfrac{2\pi}{3}\right)\end{array}\right] \tag{29e}$$

$$\begin{bmatrix} v_{ab}^N \\ v_{bc}^N \\ v_{ca}^N \end{bmatrix} = \begin{bmatrix} 1 & -1 & 0 \\ 0 & 1 & -1 \\ -1 & 0 & 1 \end{bmatrix} . \begin{bmatrix} v_a^N \\ v_b^N \\ v_c^N \end{bmatrix} \tag{30a}$$

$$v_a^N = v_1^N; v_b^N = v_2^N; v_c^N = v_3^N \tag{30b}$$

The analytical expression of the LL-Voltage $v_{ab}^N(t)$, $v_{bc}^N(t)$ and $v_{ca}^N(t)$ are given in (31), (32), and (33), respectively.

$$v_{ab}^N(t)$$

$$= k\sqrt{3} * V_{0,1}\cos\left[\omega_0 t+\frac{\pi}{6}\right] \tag{31a}$$

$$+ k\sqrt{3}\sum_{n_v=2}^{\infty} V_{0,2n_v-1}\cos\left[\left(2n_v-1\right)\left(\omega_0 t+\frac{\pi}{6}\right)\right] \tag{31b}$$

$$+ \sqrt{3}\sum_{m_v=1}^{\infty}\sum_{\substack{n_v=-\infty \\ n_v\neq 0}}^{\infty} V_{(2m_v-1),2n_v}\cos\left[\begin{array}{c}\left(2m_v-1\right)\left(\omega_c t-\theta_c\right)+ \\ 2n_v\left(\omega_0 t+\dfrac{\pi}{6}\right)\end{array}\right] \tag{31c}$$

$$+ \sqrt{3}\sum_{m_v=1}^{\infty}\sum_{n_v=-\infty}^{\infty} V_{2m_v,2n_v+1}\cos\left[\begin{array}{c}2m_v\left(\omega_c t-\theta_c\right)+ \\ \left(2n_v+1\right)\left(\omega_0 t+\dfrac{\pi}{6}\right)\end{array}\right] \tag{31d}$$

$$v_{bc}^N(t)$$

$$= k\sqrt{3} * V_{0,1}\cos\left[\omega_0 t-\frac{\pi}{2}\right] \tag{32a}$$

$$+ k\sqrt{3}\sum_{n_v=2}^{\infty} V_{0,2n_v-1}\cos\left[\left(2n_v-1\right)\left(\omega_0 t-\frac{\pi}{2}\right)\right] \tag{32b}$$

$$+ \sqrt{3}\sum_{m_v=1}^{\infty}\sum_{\substack{n_v=-\infty \\ n_v\neq 0}}^{\infty} V_{(2m_v-1),2n_v} \times \cos\left[\begin{array}{c}\left(2m_v-1\right)\left(\omega_c t-\theta_c\right)+ \\ 2n_v\left(\omega_0 t-\dfrac{\pi}{2}\right)\end{array}\right] \tag{32c}$$

$$+ \sqrt{3}\sum_{m_v=1}^{\infty}\sum_{n_v=-\infty}^{\infty} V_{2m_v,2n_v+1}\cos\left[\begin{array}{c}2m_v\left(\omega_c t-\theta_c\right)+ \\ \left(2n_v+1\right)\left(\omega_0 t-\dfrac{\pi}{2}\right)\end{array}\right] \tag{32d}$$

$$v_{ca}^N(t)$$

$$= k\sqrt{3} * V_{0,1}\cos\left[\omega_0 t+\frac{5\pi}{6}\right] \tag{33a}$$

$$+ k\sqrt{3}\sum_{n_v=2}^{\infty} V_{0,2n_v-1}\cos\left[\left(2n_v-1\right)\left(\omega_0 t+\frac{5\pi}{6}\right)\right] \tag{33b}$$

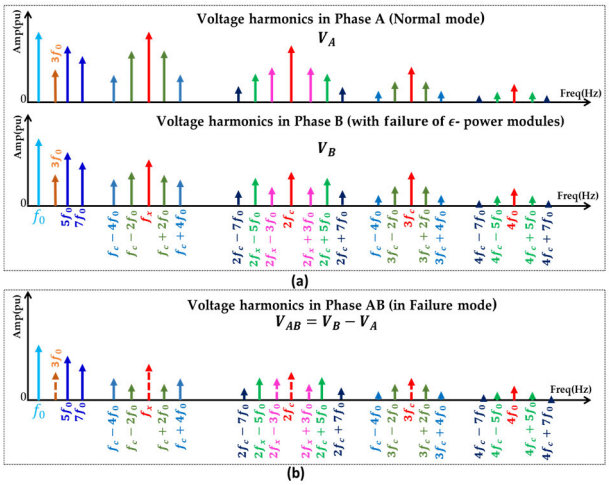

FIGURE 10. An harmonic analysis under unbalanced conditions. (a): Voltage harmonic in phase A; (b): Voltage harmonic in phase AB.

$$+ \sqrt{3}\sum_{m_v=1}^{\infty}\sum_{\substack{n_v=-\infty \\ n_v\neq 0}}^{\infty} V_{(2m_v-1),2n_v} \times \cos\left[\begin{array}{c}\left(2m_v-1\right)\left(\omega_c t-\theta_c\right)+ \\ 2n_v\left(\omega_0 t+\dfrac{5\pi}{6}\right)\end{array}\right] \tag{33c}$$

$$+ \sqrt{3}\sum_{m_v=1}^{\infty}\sum_{n_v=-\infty}^{\infty} V_{2m_v,2n_v+1} \times \cos\left[\begin{array}{c}2m_v\left(\omega_c t-\theta_c\right)+ \\ \left(2n_v+1\right)\left(\omega_0 t+\dfrac{5\pi}{6}\right)\end{array}\right] \tag{33d}$$

Figures 9(a) and 9(b), respectively illustrates the LN- and LL-voltage harmonic spectrum produced while the converter is in normal (ideal) mode. Since identical components can be found in phase B, only voltage harmonics from phase A are shown in figure 10. Three types of harmonics are depicted in figure 10a: (i) Baseband components (peru and blue lines) that are proportional to fundamental frequency f_0, (ii) Carrierband components (red lines) that are proportional to the PWM frequency f_c, and (iii) Sideband components (nevy, green and pink lines) that are centered on the carrier frequency are examples of these components.

The carrier band harmonics given in (29c) are not present in the line-to-line voltages since these components are identical across all phases as shown in figure 10b. In addition, triplen baseband and sideband harmonics are cancelled between the phase leg, as shown in figure 10b.

This conclusion is invalid when a CHB-VSI is under failure mode, i.e., when operating with failed H-bridge cells as discussed in the next sequel.

2) HARMONIC ANALYSIS IN FAILURE MODE

With the three PWM reference voltages shifted by 120°, an analytical CHB-VSI LN-voltage harmonic expressions in

failure mode are given by:

$$v_i^F(t) = k * V_{0,1}(M_i)\cos\left[\omega_0 t - (i-1)\frac{2\pi}{3}\right] \tag{34a}$$

$$+ K_i \sum_{n_v=2}^{\infty} V_{0,2n_v-1}(M_i) \times \cos\left((2n_v-1)\left(\omega_0 t - (i-1)\frac{2\pi}{3}\right)\right) \tag{34b}$$

$$+ K_i \sum_{m_v=1}^{\infty} V_{(2m_v-1),0}(M_i)\cos\left[(2m_v-1)(\omega_c t - \theta_c)\right] \tag{34c}$$

$$+ \sum_{m_v=1}^{\infty}\sum_{\substack{n_v=-\infty \\ n_v\neq 0}}^{\infty} V_{(2m_v-1),2n_v}(K_i, M_i) \times \cos\left[\begin{array}{l}(2m_v-1)(\omega_c t-\theta_c)+ \\ 2n_v\left(\omega_0 t-(i-1)\frac{2\pi}{3}\right)\end{array}\right] \tag{34d}$$

$$+ \sum_{m_v=1}^{\infty}\sum_{\substack{n_v=-\infty \\ n_v\neq 0}}^{\infty} V_{(2m_v-1),2n_v}(K_i, M_i) \times \cos\left[\begin{array}{l}(2m_v-1)(\omega_c t-\theta_c)+ \\ 2n_v\left(\omega_0 t-(i-1)\frac{2\pi}{3}\right)\end{array}\right] \tag{34e}$$

$$+ \sum_{m_v=1}^{\infty}\sum_{n_v=-\infty}^{\infty} V_{2m_v,2n_v+1}(K_i, M_i) \times \cos\left[\begin{array}{l}2m_v(\omega_c t-\theta_c)+ \\ (2n_v+1)\left(\omega_0 t-(i-1)\frac{2\pi}{3}\right)\end{array}\right] \tag{34f}$$

$$K_i = (k_i - \epsilon_i) \tag{35}$$

k : is the total number of H-bridge cells per-phase in the normal (balanced) mode, K_i: is the total number of healthy cells still present in each phase under failure mode, and ϵ_i: is the total number of failed and bypass cells per-phase. The frequency of the harmonic components in failure mode is solely dependent on the constant integers m_v and n_v., just like in normal mode. However, the magnitudes of these harmonics are dependent on the constant K_i, with respect of modulation index M_i applied in each PWM reference voltage. A harmonic analysis of a CHB-VSI operation with failed cells is discussed in figure 10, where it is assumed that the inverter is operating with ϵ-failed cells in phase B and there is no failure in phases A and C. In this case, the spectrum of line voltage V_{AC} will remain unchanged and be similar to that under normal (balanced) conditions as shown in figure 9b. Only the line voltages V_{AB} and V_{BC} spectra are impacted, and they theoretically have the same harmonic distribution. In both failure and normal modes, the CHB-VSI theoretically produces per-phase voltage harmonics at the same frequencies, while their amplitudes may vary, as can be shown in figure 10a. For instance, the magnitudes of the carrier-band harmonics are not the same all the phases. Their magnitude in phases A and B are given by the expressions $k * V_{0,2n_v-1}$ and $K_i * V_{(2m_v-1),0}(M_i)$, respectively, following (29c) and (34c). As a result, carrierband harmonics in failure mode cannot be eliminated by differentiating the LL voltages, as illustrated in figure 10b. Similarly, it can be also observed that in LL voltage spectrum, the triplen baseband (e.g., $3f_0$) and sideband (e.g., $2f_c \pm 3f_0$) are not eliminated either. A failure of H-bridge cell introduces more voltage harmonic distortion, increasing current ripple and pulsating torque components, which in turn may raise torsional vibration and mechanical stresses.

3) A LIMITATION OF THE EXISTING FAULT-TOLERANT CONTROL METHODS FOR CHB-VSI OPERATION WITH FAILED CELLS

It is feasible to balance line voltages even in situations where the phase voltage remains unbalanced, through the use of appropriate fault-tolerant control methods. This can be achieved by modifying the inverter reference voltage phase angles. Such an approach offers a reliable and effective means of achieving optimal voltage balance. However, the CHB-VSI output voltage and current spectra still need to be improved even by adequately adjusting the inverter reference voltage phase angles. For instance, it has been demonstrated in the previous subsection that all carrier band, triple baseband, and sideband harmonics in failure mode do not cancel between the phase legs as in normal mode, resulting in a poorer LL-voltage harmonic spectrum. The motor impedance converts these undesirables' voltage harmonics to current harmonics. And when combined, generated voltage and current harmonics will produce undesirable torque components that may result in harmonic pollution and even harmonic resonance. Evaluation, then cancellation of these undesired harmonic components, is essential to reduce torsional stresses and maintain a safe and stable system operation of a PSH plant.

VI. TORSIONAL STRESSES INDUCED BY THE INVESTIGATED VFDS

A. GENERAL CONSIDERATIONS

The shaft connected to the electrical machine in all VFD configurations is the same for all investigated cases. This assumption will provide an identical basis for comparison of torsional stresses generated by all investigated VFDs. In that case, torsional stress components are identical to the torque components relative to their magnitudes.

B. ELECTRICAL HARMONIC AND THEIR INDUCED TORSIONAL STRESSES

1) BASIC CONSIDERATIONS

The generic torque equations provided from (9) to (15) are used to evaluate frequencies and magnitudes of torsional stress components for a given VFD. Equation (14) shows all

families of harmonic frequencies which might have relevant magnitudes. They solely depend on the integers n_v and the set (m_i, n_i) . The combination of these integers depends on the VFD topology, the type of PWM strategy, and the selected sampling method [49]. The set (m_i, n_i) is derived from voltage set (m_v, n_v). The most crucial step for practicing engineers is to determine the appropriate mix of (m_v, n_v) for each VFD topology and the corresponding PWM strategies based on the final combination of the drive system. For example, developments for a parallel connection of VFDs with synchronized or interleaved PWM signals are provided, as well as multi-three-phase machines, as discussed in the earlier section.

2) TORSIONAL STRESSES INDUCED BY ELECTRICAL HARMONICS

The following torsional stresses (36)-(38) and their sources of electrical (voltage and current) harmonic families are found in all investigated VFDs. The asymmetrical regular sampled PWM method, with double-edge triangular carriers, is analyzed because this method produces superior harmonic quality and is the most used in high-power VFDs, and carriers are in phase for multilevel inverters [49].

1) Torsional stresses from electrical fundamental and baseband harmonics:

$$t_{e_{0,6n}}(t) = T_{eDC} + \sum_{n=0}^{\infty} T_{e_{0,6n}} \cos\left(6n\omega_0 t\right) \tag{36}$$

1) Torsional stresses from sidebands around even multiple of carrier frequency of electrical harmonics:

$$t_{e_{2m,\pm 6n}}(t) = \sum_{m=1}^{\infty}\sum_{n=0}^{\infty} T_{e_{2m,6n}} \cos\left(2m\omega_c t \pm 6n\omega_0 t\right) \tag{37}$$

1) Torsional stresses from sidebands around odd multiple of carrier frequency of electrical harmonics:

$$t_{e_{2m,\pm 2n}}(t) = \sum_{m=1}^{\infty}\sum_{\substack{n=-\infty \\ (n\neq 0)}}^{\infty} T_{e_{2m,2n-1}} \times \cos\left[(2m-1)\,\omega_c t \pm (2n-1)\,\omega_0 t\right] \tag{38}$$

VII. VALIDATIONS BY NUMERICAL SIMULATIONS

A. SYSTEM SETUP AND VALIDATION

A two-level, three-level NPC, and seven-level CHB VSI have been simulated by supplying a 35 MVA induction machine. Only the steady state is of interest for the harmonic analysis. The asymmetrical regular sampled PWM method has been implemented with two vertically phase-shifted double-edge triangular carriers for the NPC. The two-level inverter has one carrier signal. The carrier frequency is chosen at a relatively low value for validation purposes, $f_c = 1kHz$. For each configuration, two identical VFDs are parallel connected through a set of three-phase coupling inductances of $3mH$. The PWM commands of both modules are first synchronized, then interleaved with a phase $\theta_c = \pi/2$ according to (18). The system is simulated for fundamental frequencies, f_0, from 10 Hz to the nominal frequency of 65 Hz, with a step of 5 Hz. Then, the machine's voltages, currents, and torque are extracted in the time-domain for analysis. Since the paper focuses exclusively on analyzing and discussing the steady-state performances of PSH-VSI systems, simulation results are collected to ensure an accurate harmonic analysis in the frequency domain until each system attains its steady state. Also, the effects of system controllers (Such as PI, and PID) are not investigated. They have a minor influence on this type of analysis because they mainly act on system transient dynamics, damping transient oscillation resulting from the system dynamic changes. An analysis of motor voltage, current, and torque harmonics under normal, failure and corrected modes is also conducted for the specific case of CHB-VSI topology. A corrected operating mode of the system is the operation of the CHB-VSI system with failed cells modulated with the neutral-shift-based PWM method developed in [40], [46], [47], [48], [49], [50], [51], [52]. The results are post-processed by calculating their Fast Fourier Transform (FFT). The harmonic frequencies are extracted, and dominant components are identified and compared to the theoretical predictions. The time domain torsional stress is reconstructed based on dominant components only. The torsional stress is calculated, assuming the shaft has the same mechanical parameters. Finally, the locations of all the simulated torsional stresses of all operating points are laid over to the theoretical lines of their corresponding Campbell diagrams. This interference diagram helps to predict which

TABLE 1. Families of VFD-induced torque harmonics.

Fundamental and baseband harmonics				
$(\mathbf{m},\mathbf{n})$	Voltage/ Current	Torque	2x Interleaved	2x three-phase systems
(0,1)	ω_0	0	0	0
(0,5)	$5\omega_0$	$6\omega_0$	$6\omega_0$	Cancelled
(0,7)	$7\omega_0$			
(0,11)	$11\omega_0$	$12\omega_0$	$12\omega_0$	$12\omega_0$
(0,13)	$13\omega_0$			
Carrier band and sideband harmonics around odd multiple of carrier frequency				
(1,0)	ω_c	None	None	
(1,2)	$\omega_c \pm 2\omega_0$	$\omega_c \pm 3\omega_0$	$\omega_c \pm 3\omega_0$	$\omega_c \pm 3\omega_0$
(1,4)	$\omega_c \pm 4\omega_0$			
(1,6)	$\omega_c \pm 6\omega_0$	None	None	None
(1,8)	$\omega_c \pm 8\omega_0$	$\omega_c \pm 9\omega_0$	$\omega_c \pm 3\omega_0$	$\omega_c \pm 3\omega_0$
(1,10)	$\omega_c \pm 10\omega_0$			
Carrier band and sideband harmonics around even multiple of carrier frequency				
(2,0)	None	None	None	
(2,1)	$2\omega_c \pm \omega_0$	$2\omega_c$	Cancelled	$2\omega_c$
(2,3)	$2\omega_c \pm 3\omega_0$	None	None	
(2,5)	$2\omega_c \pm 5\omega_0$	$2\omega_c \pm 6\omega_0$	Cancelled	Cancelled
(2,7)	$2\omega_c \pm 7\omega_0$			
(2,9)	$2\omega_c \pm 9\omega_0$	None		
(2,11)	$2\omega_c \pm 11\omega_0$	$2\omega_c \pm 12$	Cancelled	$2\omega_c \pm 12$
(2,13)	$2\omega_c \pm 13\omega_0$			

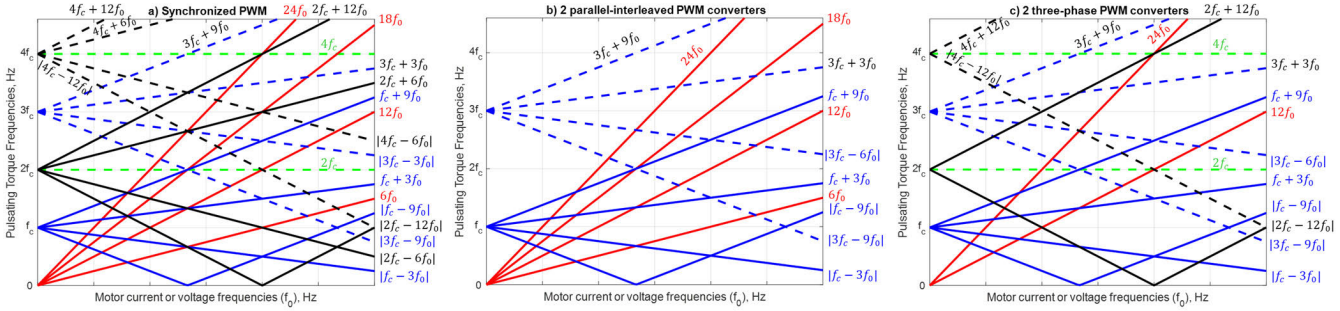

FIGURE 11. Campbell diagrams of VFDs with (a) synchronized PWM commands; (b) parallel-interleaved PWM commands, and (c) two three-phase systems supplied by synchronized PWM commands.

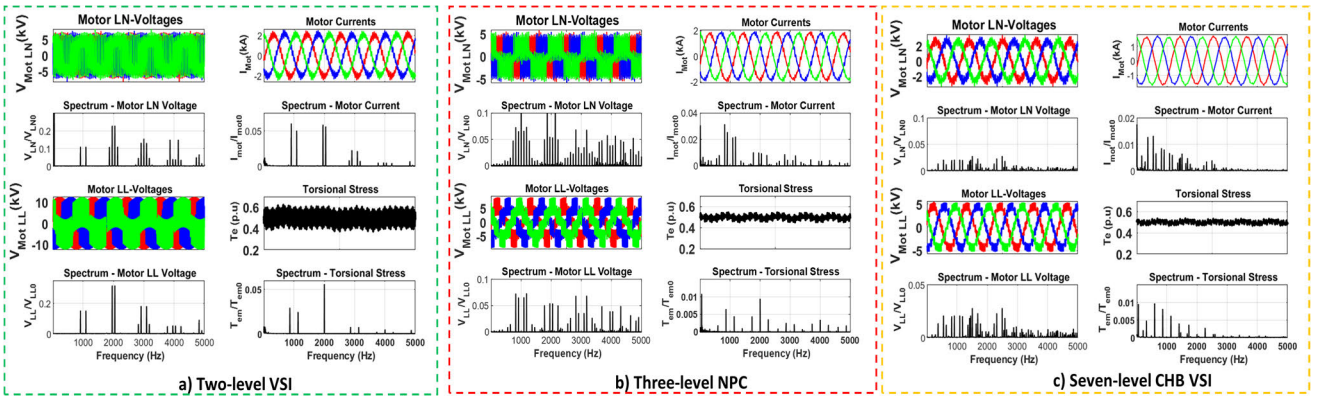

FIGURE 12. Simulations result of parallel VSIs with synchronized PWM;f_c = 1kHz; f_0 = 45Hz.

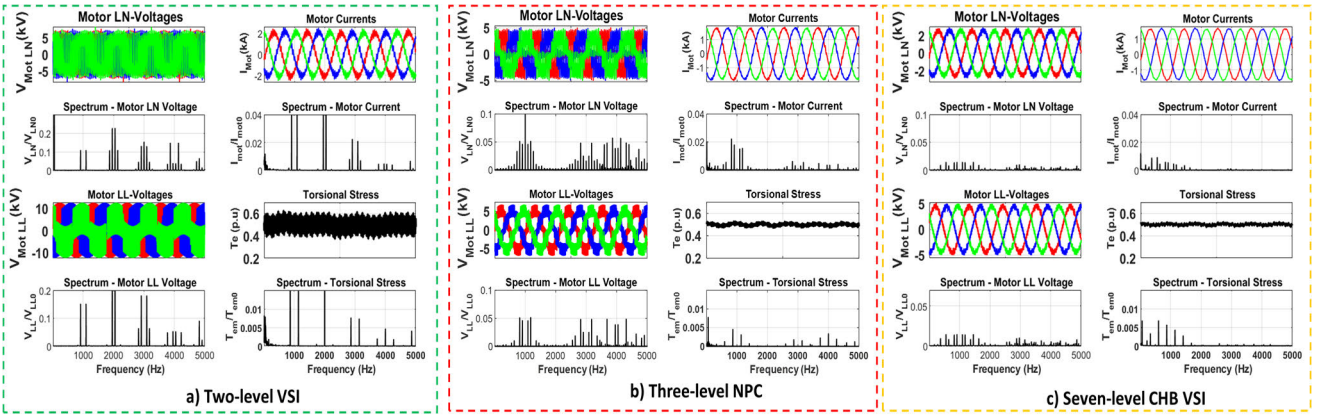

FIGURE 13. Simulations result of parallel VSIs with $\theta_c = \pi/2$ interleaved PWM;f_c = 1kHz; f_0 = 45Hz.

operating point may induce threatening torsional stress for each system, potentially leading to a reduced lifetime of mechanical components.

B. SIMULATION RESULTS AND DISCUSSIONS

More than 75 operating points have been simulated. The detailed results of two representative cases, where $f_c = 1\ kHz$ and $f_0 = 45kHz$ are discussed for three types of converters. The remaining results are summarized in the respective Campbell diagrams. Figure 11 shows the motor voltages, currents, and torsional stresses for synchronized (figure 11a), interleaved PWM commands of a parallel connection (figure 11b), and of the three investigated VSI (figure 11c). In figures 12 and 13, both time and frequency domain results are shown for each state variable. Precise locations of their respective torsional stresses are shown in figure 14. The frequencies are consistent with the theoretical results shown in Table 1, and in (9) and (12). The spectra of

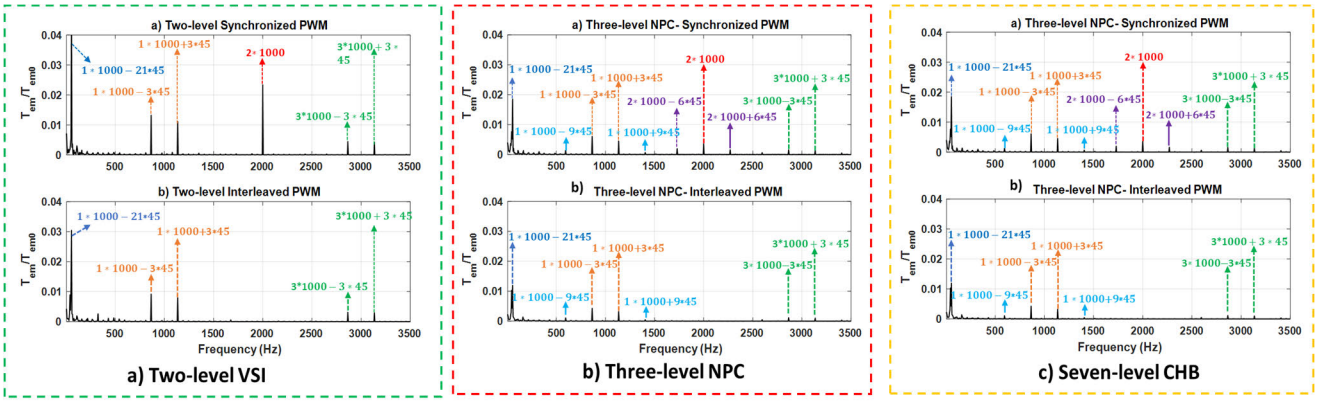

FIGURE 14. Precise location of torsional stresses for both synchronized and $\theta_c = \pi/2$ interleaved PWM different VSIs.

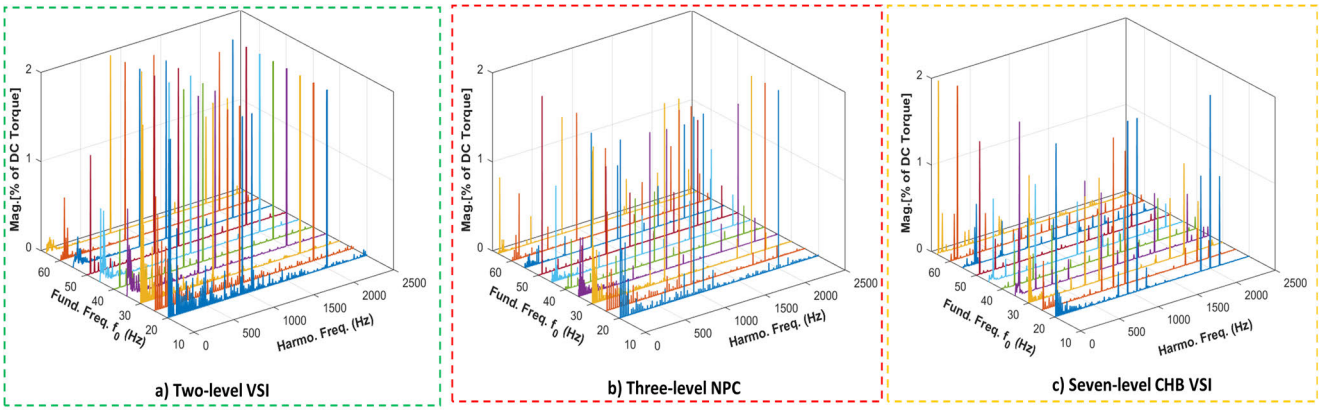

FIGURE 15. Simulation results with synchronized PWM;f_c = 1kHz; f_0 = 45Hz.

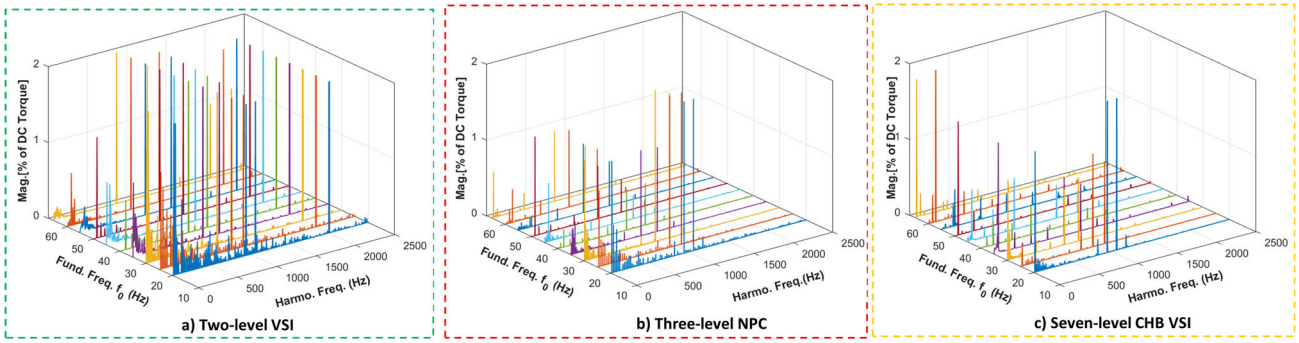

FIGURE 16. Simulation results with $\theta_c = \pi/2$ interleaved PWM;f_c = 1kHz; f_0 = 45Hz.

the torsional stress over the full operating speed range of the investigated VFDs under synchronized and interleaved PWM methods are shown in figure 15 and figure 16, respectively. As indicated in Section IV-C, classes of harmonics that are cancelled are sideband around even multiple of the carrier frequency (2,000 Hz). This is valid for all the investigated converters. The interference diagrams for each of the systems are shown in figure 17 in the form of Campbell diagrams. The red dots show the location of torque components for synchronized PWM commands, while the greens show the one for the interleave commands. As discussed in Section IV-C, no green dot appears on sideband lines around odd multiple of the carrier frequency.

C. SELECTED SIMULATION RESULTS FROM A CHB-VSI SYSTEM WITH FAILED CELLS

The simulations were performed on a three-phase, nine-cell CHB-VSI system (three cells in each phase), where two faulty and bypassed power cells were placed at phase *A*. The gating signals for power switches are produced using the

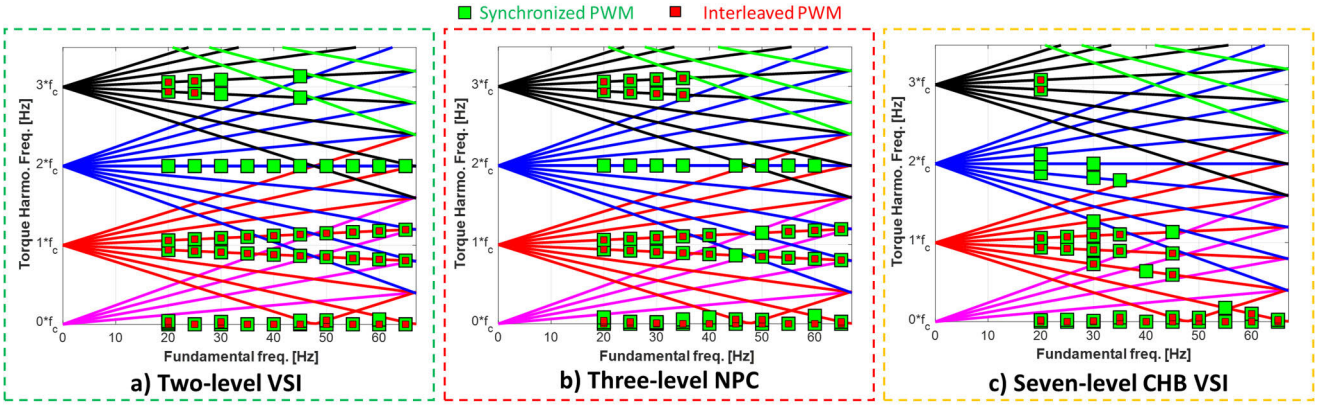

FIGURE 17. Generated Campbell diagrams of each investigated VSI topologies.

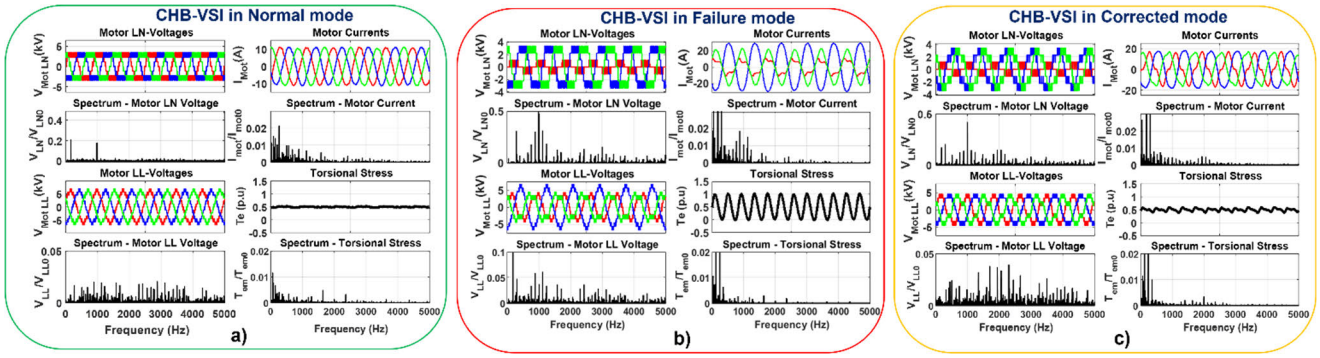

FIGURE 18. Simulation results a CHB-VSI at different operating mode with; v_a = [001]; v_b = [111] and v_c = [111]. (a): CHB-VSI in coral mode; (b) CHB-VSI in failure mode; (c): CHB-VSI in corrected mode.

conventional phase disposition (PD-PWM) control method in both the failure operation (without the neutral shift method) and the corrected mode (with the neutral shift method). The selected simulation results are discussed in figure 18.

The results in normal mode are shown in figure 18a on the left, the results in failure mode are shown in figure 18b, and the results in corrected mode are shown in figure 18c on the right. In normal mode, balanced voltage and currents are applied at the motor terminal. When two power cells fail, the voltage waveform V_A drops by two levels and unwanted harmonic distortions are introduced in both motor phase and line voltages. The resulting unbalanced and distorted motor currents, as a result, cause torque pulsation, which may increase vibration and mechanical stress. The neutral shift-based control method is introduced in corrected mode to maximize and balance the line voltages. In this condition, the phase angles of the voltages have been adjusted so that inverter phase A is displaced from phase B and from phase C by 140.4°. This adjustment has successfully rebalanced the motor line voltages and improved the current and torque waveforms [figure 18c] compared to the failure mode [figure 18b]. However, it can be observed that the neutral-shift method did not eliminate the undesirable harmonics that the failure introduced. Figure 19 shows a zoom on the CHB-VSI-

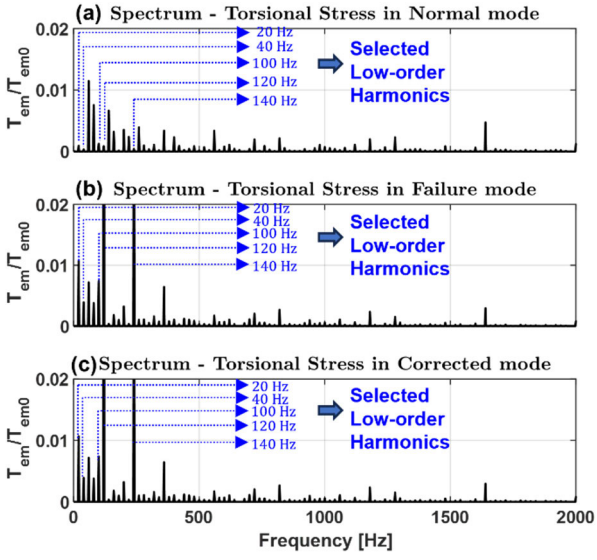

FIGURE 19. Zoom in CHB-VSI induced torsional stresses (a) Normal mode; (b) Failure mode; (c) Corrected mode.

induced torsional stresses in normal mode, failure mode, and corrected mode. It is observed that, the magnitudes of some low-order harmonics in normal mode [figure 19a] have been

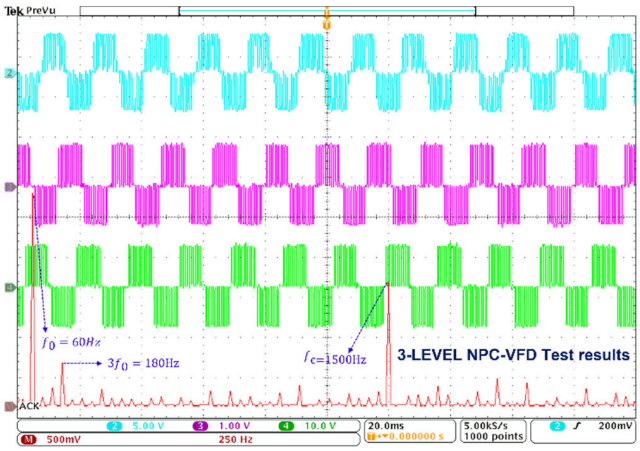

FIGURE 20. Synchronized switched waveforms obtained from a single 3-level NPC VFD; $f_c = 1.5$ kHz; $f_0 = 60$Hz.

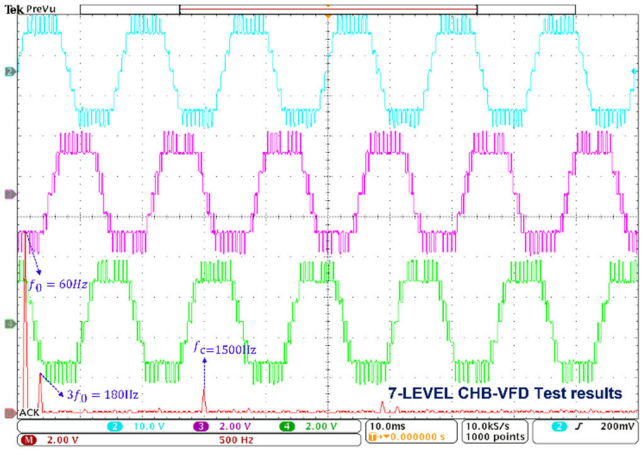

FIGURE 21. Synchronized switched waveforms obtained from a single 7-level CHB VFD; $f_c = 1.5$ kHz; $f_0 = 60$Hz.

seen to significantly rise in failure mode [figure 19b]. These unwanted harmonics are also present in corrected mode, as shown in [figure 19c], at the same frequency positions. This result shows that, it is crucial for the completeness of the design to evaluate the type of pulsating torque components the CHB-VSI system generates in the motor's airgap under unbalanced conditions, even controlled by a given fault-tolerant control technique. Such an analysis is beneficial to track and quantify the VFD-induced harmonics in order to ensure the integrity of the system over the operational envelop.

D. HYBRID EXPERIMENTAL-NUMERICAL RESULTS AND DISCUSSIONS

Hybrid experimental–numerical real-time simulations are conducted to verify the accuracy and consistency of the suggested theoretical developments. This type of validation involves combining real-time physical experiments with numerical simulation to analyze the behavior of the PSH system model. Voltage measurements from a reduced-scaled lab prototype with a 3-level NPC and 7-level CHB were used to supply a numerical induction motor model. A Simulink real-time target PC equipped with a DAQ board PCI 6229 was used to connect each VFD power stage to the numerical simulation. This enables data exchange between the physical (real/analogical) and numerical/digital system model parts. Examples of experimental synchronized voltage waveforms used for the hybrid experimental–numerical validations are shown in figures 20 and 21.

Sample hybrid experimental-numerical results are summarized in figure 22a-b, where motor voltage, current, and torque waveforms and their corresponding spectra are provided when supplied by collected 3-level NPC and 7-level CHB voltage measurements. The exact locations of pertinent voltage and current harmonic components induced by each VFD topology are highlighted based on the actual value of the fundamental and carrier frequencies. That helps to show the family type of pulsating torque components they generate in the motor's airgap. It should be noted that the fundamental component has been removed in each motor voltage and current spectrum for a more precise analysis of harmonic locations. Examples of the 3-level NPC VFD-induced torsional stress components extracted from figure 22a are summarized in Table 2, while those generated by the 7-level CHB VFD [figure 22b] are outlined in Table 3. In both situations, it can be observed that all the torque

TABLE 2. Example of motor air-gap torque harmonic families from a 3-Level NPC VSI system model.

3-Level NPC VFD-Induced Torsional Stresses [Figure 22(a4)-(a6)]			
Current harmonics		Induced Torque harmonics	
Fundamental and baseband			
(3,0)	180 Hz = 3×60 Hz	(4,0)	240 Hz = 4×60Hz
(5,0)	300 Hz = 5×60 Hz		
Sideband harmonics around odd multiple of Carrier frequency			
(1, -4)	1260 Hz = |1×1500-4×60|	(1, -3)	1320 Hz= |1×1500-3×60|
(1, -2)	1380 Hz = |1×1500-2×60|		
(1, 2)	1620 Hz = |1×1500+2×60|	(1, 3)	1680 Hz= |1×1500+3×60|
(1, 4)	1740 Hz= |1×1500+4×60|		
Sideband harmonics around even multiple of Carrier frequency			
(2, -7)	2580 Hz = |2×1500-7×60|	(2, -6)	2640 Hz= |2×1500-6×60|
(2, -5)	2700 Hz = |2×1500-5×60|		
(2, 5)	3300 Hz = |2×1500+5×60|	(2, 6)	3360 Hz= |2×1500+6×60|
(2, 7)	3420 Hz = |2×1500+7×60|		

TABLE 3. Example of motor air-gap torque harmonic families from a 7-Level CHB VSI system model.

7-Level CHB VFD-Induced Torsional Stresses [Figure 22(b4)-(b6)]			
Current harmonics		Induced Torque harmonics	
Baseband harmonics			
(7,0)	420 Hz = 7×60 Hz	(8,0)	480 Hz = 8×60Hz
(9,0)	540 Hz = 9×60 Hz		
Sideband harmonics around odd multiple of Carrier frequency			
(1, -4)	1260 Hz = |1×1500-4×60|	(1, -3)	1320 Hz= |1×1500-3×60|
(1, -2)	1380 Hz = |1×1500-2×60|		
(1, 0)	1500 Hz	(1, 1)	1560 Hz= |1×1500+1×60|
(1, 2)	1620 Hz= |1×1500+2×60|		
Sideband harmonics around even multiple of Carrier frequency			
(2, 5)	3300 Hz = |2×1500+5×60|	(2, 6)	3360 Hz= |2×1500+6×60|
(2, 7)	3420 Hz = |2×1500+7×60|		

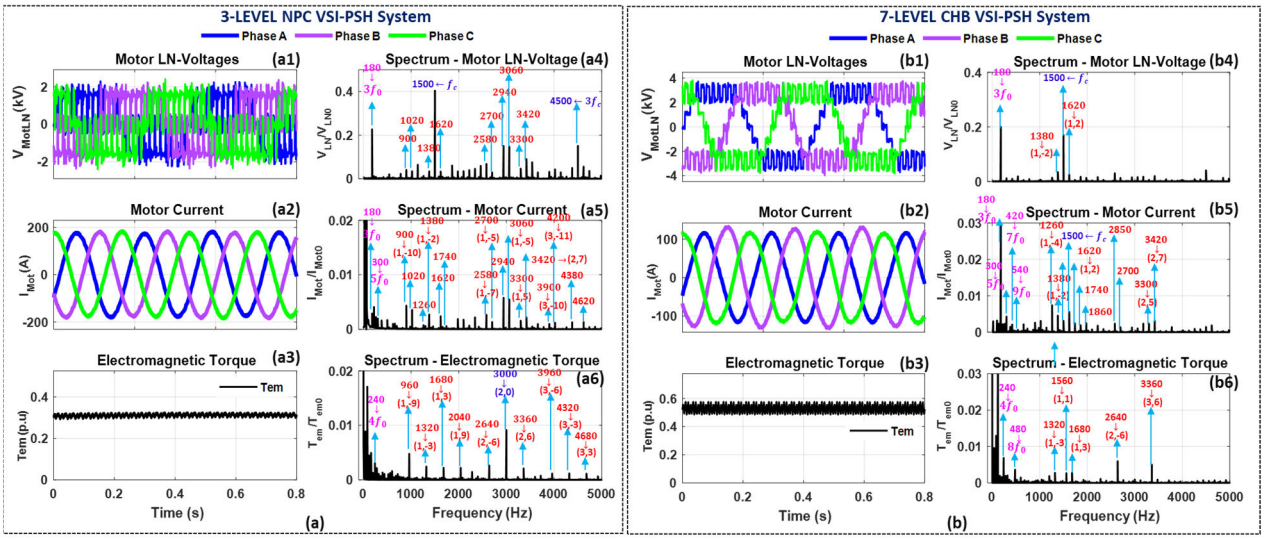

FIGURE 22. Sample Hybrid Experimental-Numerical Simulation results. (a): Results a 3-Level NPC VSI system; (b) Results a 7-Level CHB VSI system.

harmonics generated are related to the harmonics produced by the VFD-induced currents, which can be expressed in terms of baseband and sideband components.

The analysis reveals that two current harmonic components produce each fluctuating torque harmonic component, as predicted by the analytical expression provided in Section IV. A clear understanding of how torque is generated by voltage/current harmonics applied to the motor inputs is crucial in developing a Campbell diagram for a particular VFD topology to identify the operational motor speeds or fundamental frequencies where torsional excitation may occur.

VIII. CONCLUSION

A simple method to extract relevant electromagnetic torque components in a motor airgap supplied by VFDs has been developed in this paper. It is based on a torque expression in the stationary and orthogonal reference frame and is suitable for both induction and synchronous motors. The Campbell lines of any inverter can be quickly mapped out when basic parameters such as the PWM carrier frequency and the machines operating range are known. The accuracy of the method has been confirmed on four parallel-connected two-level, NPC, and CHB VFD topologies, where simulation results match theoretical developments. The analysis and evaluation of the effects of VSI-induced harmonics on motor airgap pulsating torques under unbalanced conditions have been also conducted. The theoretical foundations presented in this paper are intended to improve the understanding of PSH shaft element lifetime. More importantly, they are crucial for practicing engineers involved in the integration of large rotating shaft and performing torsional analysis as required per API 617, 672 and 673 standards for example. Therefore, the results of this investigation can be extended to other applications, such as large compressor drivetrains that are found in the oil and gas industry, or in milk and paper industry. The study enables the possibility to accurately predict the accelerated wear, fatigue, and premature failure of shaft mechanical elements. However, the study has some limitations that need further investigation.

1) The proposed study has been limited to conventional voltage source converters (VSCs) such as two-level, three-level neutral-point clamped, and seven-level cascaded H-bridge converters. However, it is essential to investigate the suitability and applicability of the proposed research in other VSCs, such as modular multilevel converters, which offer potential advantages for variable-speed PHSP applications compared to conventional power conversion technologies.
2) There are substantial incentives to decarbonize other industries that may utilize high-power variable speed drive systems (VSDSs) similar to the ones investigated in this paper. For example, in the oil and gas industry, large steam and gas turbines driving compressors are increasingly being replaced by VFDs and motors. The power can easily reach 100MW. Consequently, the integration of the VSDS system into compressor drivetrains induces the risk to exciting the shaft Eigen modes. This paper does not cover learnings from other industrial applications.
3) The analysis in the paper is limited to the PSH system configuration depicted in Figure 6b, which employs a reversible power converter driving an induction machine. However, extending this study to the PSH system configuration shown in Figure 6c is also essential, which involves using a Doubly fed induction machine (DFIM) that requires special attention in actual industrial Pumped Hydropower Storage sys-

tems. It is necessary to derive and discuss time-domain analytical expressions for the instantaneous pulsating torque components in a DFIM air gap when supplied by back-to-back VSIs.

REFERENCES

[1] M. Alathamneh, H. Ghanayem, E. Muljadi, and R. M. Nelms, "A comparative study of conventional pumped-storage hydropower (C-PSH) and ternary pumped-storage hydropower (T-PSH) systems integrated with wind generation," in *Proc. 4th Int. Conf. High Voltage Eng. Power Syst. (ICHVEPS)*, Aug. 2023, pp. 630–635.

[2] U.S. Department of Energy. (Jan. 5, 2023). *Hydropower Basics*. [Online]. Available: https://www.energy.gov/eere/water/hydropower-basics

[3] R. Uria-Martinez, M. Johnson, and R. Shan, "Hydropower market report," Dept. Energy, Washington, DC, USA, Rep. doe/ee-2088, 2021.

[4] V. Koritarov, Q. Ploussard, J. Kwon, and P. Balducci, "A review of technology innovations for pumped storage hydropower," Argonne Nat. Lab., Tech. Rep. ANL-22/08, 2022, doi: 10.2172/1867238.

[5] R. K. Mohanta, T. R. Chelliah, S. Allamsetty, A. Akula, and R. Ghosh, "Sources of vibration and their treatment in hydro power stations—A review," *Eng. Sci. Technol., Int. J.*, vol. 20, no. 2, pp. 637–648, Apr. 2017.

[6] W. Guo and F. Wu, "Hydraulic-mechanical coupling vibration performance of pumped storage power station with two turbine units sharing one tunnel," *J. Energy Storage*, vol. 53, Sep. 2022, Art. no. 105082.

[7] I. Ahmad, A. Rashid, I. Ahmad, and A. Rashid, "On-line monitoring of hydro power plants in Pakistan," *Inf. Techn. J.*, vol. 6, no. 6, pp. 919–923, 2007.

[8] D. Momčilović, Z. Odanović, R. Mitrović, I. Atanasovska, and T. Vuherer, "Failure analysis of hydraulic turbine shaft," *Eng. Failure Anal.*, vol. 20, pp. 54–66, Mar. 2012.

[9] Y. Thakur, G. Goga, and V. Shrivastava, "A review study on the improvement of stator frame design and prediction of electromagnetic vibration of hydro generators," *Mater. Today, Proc.*, vol. 102, pp. 96–110, Jan. 2023.

[10] E. Georgievskaia, "Destruction of the hydraulic unit shaft: Why it is possible," *Forces Mech.*, vol. 4, pp. 1–10, Oct. 2021.

[11] R. M. Pindoriya, R. K. Thakur, B. S. Rajpurohit, and R. Kumar, "Numerical and experimental analysis of torsional vibration and acoustic noise of PMSM coupled with DC generator," *IEEE Trans. Ind. Electron.*, vol. 69, no. 4, pp. 3345–3356, Apr. 2022.

[12] W. Zhao, Q. He, W. Tian, Y. Sun, and J. Ji, "Investigation of winding configuration on electromagnetic vibration in modular dual three-phase PM machine," *IEEE Trans. Ind. Electron.*, vol. 71, no. 2, pp. 1257–1267, 2024.

[13] J. Song-Manguelle, S. Schroder, T. Geyer, G. Ekemb, and J. M. Nyobe-Yome, "Prediction of mechanical shaft failures due to variable frequency drives," *IEEE Trans. Ind. Appl.*, vol. 25, no. 4, pp. 130–138, Jan. 2010.

[14] G. Ekemb, F. Slaoui-Hasnaoui, J. Song-Manguelle, P. M. Lingom, and I. Fofana, "Instantaneous electromagnetic torque components in synchronous motors fed by load-commutated inverters," *Energies*, vol. 14, no. 11, p. 3223, May 2021.

[15] M. Rossi, K. Elshawarby, M. Bruha, M. Mauri, M. S. Carmeli, and F. Castelli-Dezza, "Performance evaluation methods for VSD control systems affected by torsional vibrations: Sensitivity and energetic analyses," in *Proc. Int. Conf. Clean Electr. Power (ICCEP)*, Jul. 2019, pp. 605–610.

[16] *Axial and Centrifugal Compressors and Expander-compressors*, API Standard 617, 8th ed., Amer. Petroleum Inst., Aug. 2016.

[17] *Packaged, Integrally Geared Centrifugal Air Compressors for Petroleum, Chemical, and Gas Industry Services*, API American Petroleum Institute API Standard 672, 4th ed., Amer. Petroleum Inst., Jul. 2010.

[18] *Centrifugal Fans for Petroleum, Chemical, and Gas Industry Services*, API American Petroleum Institute API Standard 672, 3rd ed., Amer. Petroleum Inst., Dec. 2014.

[19] S. P. Betoka-Onyama, P. M. Lingom, H. Hamza, J. Song-Manguelle, M. L. Doumbia, S. Kennedy, C. Radke, W. Manfoumbi, K. Ehman, and K. Olson, "A tool for power quality assessment in electric submersible pump systems with variable frequency drives," in *Proc. Soc. Petroleum Engineers (SPE) Guld Coast Section-Electric Submersible Pump Workshop*, Woodlands, TX, USA, Oct. 2023.

[20] T. Joseph, S. Balasubramaniam, G. Li, J. Liang, W. Ming, A. Moon, K. Smith, and J. Yu, "Dynamic average converter model for MVDC link harmonic analysis," in *Proc. IEEE Milan PowerTech*, Jun. 2019, pp. 1–6.

[21] T. Joseph, W. Ming, G. Li, J. Liang, A. Moon, K. Smith, and J. Yu, "Analysis of harmonic transfer through an MVDC link," in *Proc. 15th IET Int. Conf. AC DC Power Transmiss. (ACDC)*, Feb. 2019, pp. 1–6.

[22] T. Sahrakorpi, A. Khosravi, and M. E. H. Assad, "Design and performance optimization of renewable energy systems," in *Hydropower*, vol. 6. New York, NY, USA: Academic, 2021, ch. 12, pp. 181–194.

[23] P. M. Lingom, J. Song-Manguelle, S. P. Betoka-Onyama, J. M. Nyobe-Yome, and M. L. Doumbia, "A power quality assessment of electrical submersible pumps fed by variable frequency drives under normal and failure modes," *Energies*, vol. 16, no. 4, pp. 1–34, Jul. 2023.

[24] H. Wang, O. Ahmed, B. Brennan, and B. Bellgraph, "Developing a digital twin for hydropower systems—An open platform framework," *J. Waterpower Dam Construct. Mag.*, vol. 81, no. 3, pp. 24–28, Nov. 2021.

[25] A. Mirza, W. Chen, A. Bazzi, H. Nguyen, Y. Cao, and L. Hao, "Modeling electrical aging of polyimide Kapton HN under high-voltage high-frequency pulse waveforms," *IEEE Trans. Dielectr. Electr. Insul.*, vol. 29, no. 6, pp. 2394–2401, Dec. 2022.

[26] G. C. Montanari and L. Simoni, "Aging phenomenology and modeling," *IEEE Trans. Electr. Insul.*, vol. 28, no. 5, pp. 755–776, Oct. 1993.

[27] *Evaluation, and Identification of Electrical Insulation Systems. Part 1: General Principles and Guide To Application*, IEC Standard TC 63, Section 75, 1992.

[28] *IEEE Guide for Multifactor Stress Functional Testing of Electrical Insulation Systems*, IEEE Standard 1064, 1991.

[29] M. A. Miner, "Cumulative damage in fatigue," *J. Appl. Mech.*, vol. 12, no. 3, pp. 159–164, May 1945.

[30] K. Hectors and W. De Waele, "Cumulative damage and life prediction models for high-cycle fatigue of metals: A review," *Metals*, vol. 11, no. 2, pp. 204–232, Jan. 2021.

[31] F. Conti, C. Conese, M. Colombo, L. Maggioni, G. Moschioni, and M. Tarabini, "Vibration signals for condition based maintenance of hydraulic valves," in *Proc. IEEE Int. Workshop Metrol. Ind. 4.0 IoT (MetroInd4.0&IoT)*, Jun. 2021, pp. 259–263.

[32] R. Alimardani, A. Rahideh, and S. Hedayati-kia, "Mixed eccentricity fault detection for induction motors based on time synchronous averaging of vibration signals," *IEEE Trans. Ind. Electron.*, vol. 71, no. 3, pp. 3173–3181, 2024.

[33] B. Akin, S. Choi, U. Orguner, and H. A. Toliyat, "A simple real-time fault signature monitoring tool for motor-drive-embedded fault diagnosis systems," *IEEE Trans. Ind. Electron.*, vol. 58, no. 5, pp. 1990–2001, May 2011.

[34] M. El Hachemi Benbouzid, "A review of induction motors signature analysis as a medium for faults detection," *IEEE Trans. Ind. Electron.*, vol. 47, no. 5, pp. 984–993, Oct. 2000.

[35] X. Han and A. B. Palazzolo, "VFD machinery vibration fatigue life and multilevel inverter effect," *IEEE Trans. Ind. Appl.*, vol. 49, no. 6, pp. 2562–2575, Nov. 2013.

[36] D. G. Dorrell, W. T. Thomson, and S. Roach, "Analysis of airgap flux, current, vibration signals as a function of the combination of static and dynamic air gap eccentricity in 3-phase induction motors," *IEEE Trans. Ind. Appl.*, vol. 33, no. 1, pp. 24–34, Jan./Feb. 1997.

[37] B. Akin, U. Orguner, H. A. Toliyat, and M. Rayner, "Low order PWM inverter harmonics contributions to the inverter-fed induction machine fault diagnosis," *IEEE Trans. Ind. Electron.*, vol. 55, no. 2, pp. 610–619, Feb. 2008.

[38] L.-C. Tsai, "Design and implementation of a three-section transmission line transformer," *Iranian J. Sci. Technol., Trans. Electr. Eng.*, vol. 43, no. S1, pp. 61–66, Jul. 2019.

[39] C. M. Ong, *Dynamic Simulation of Electric Machinery Using MATLAB/Simulink*. Upper Saddle River, NJ, USA: Prentice-Hall, 1999.

[40] P. M. Lingom, J. Song-Manguelle, M. L. Doumbia, R. C. C. Flesch, and T. Jin, "Electrical submersible pumps: A system modeling approach for power quality analysis with variable frequency drives," *IEEE Trans. Power Electron.*, vol. 37, no. 6, pp. 7039–7054, Jun. 2022.

[41] J. Song-Manguelle, G. Ekemb, D. L. Mon-Nzongo, T. Jin, and M. L. Doumbia, "A theoretical analysis of pulsating torque components in AC machines with variable frequency drives and dynamic mechanical loads," *IEEE Trans. Ind. Electron.*, vol. 65, no. 12, pp. 9311–9324, Dec. 2018.

[42] K. R. Vasudevan, V. K. Ramachandaramurthy, G. Venugopal, J. B. Ekanayake, and S. K. Tiong, "Variable speed pumped hydro storage: A review of converters, controls and energy management strategies," *Renew. Sustain. Energy Rev.*, vol. 135, Jan. 2021, Art. no. 110156.
[43] A. Joseph and T. R. Chelliah, "A review of power electronic converters for variable speed pumped storage plants: Configurations, operational challenges, and future scopes," *IEEE J. Emerg. Sel. Topics Power Electron.*, vol. 6, no. 1, pp. 103–119, Mar. 2018.
[44] D. L. Mon-Nzongo, G. Ekemb, J. Song-Manguelle, P. G. Ipoum-Ngome, T. Jin, and M. L. Doumbia, "LCIs and PWM-VSIs for the petroleum industry: A torque oriented evaluation for torsional analysis purposes," *Trans. Power Elec.*, vol. 34, no. 9, pp. 8956–8970, Sep. 2019.
[45] S. Schroder, P. Tenca, T. Geyer, P. Soldi, L. J. Garces, R. Zhang, T. Toma, and P. Bordignon, "Modular high-power shunt-interleaved drive system: A realization up to 35 MW for oil and gas applications," *IEEE Trans. Ind. Appl.*, vol. 46, no. 2, pp. 821–830, Jan. 2010.
[46] P. W. Hammond, "Enhancing the reliability of modular medium-voltage drives," *IEEE Trans. Ind. Electron.*, vol. 49, no. 5, pp. 948–954, Oct. 2002.
[47] F. Carnielutti, H. Pinheiro, and C. Rech, "Generalized carrier-based modulation strategy for cascaded multilevel converters operating under fault conditions," *IEEE Trans. Ind. Electron.*, vol. 59, no. 2, pp. 679–689, Feb. 2012.
[48] P. M. Lingom, J. Song-Manguelle, D. L. Mon-Nzongo, R. C. C. Flesch, and T. Jin, "Analysis and control of PV cascaded H-bridge multilevel inverter with failed cells and changing meteorological conditions," *IEEE Trans. Power Electron.*, vol. 36, no. 2, pp. 1777–1789, Feb. 2021.
[49] P. Lingom, J. Song-Manguelle, S. P. Betoka-Onyama, M. L. Doumbia, J. M. Nyobe-Yome, and T. Jin, "A generalized modulation strategy for a cascaded H-bridge multilevel inverter under unequal DC sources," in *Proc. IEEE Energy Convers. Congr. Expo. (ECCE)*, Detroit, MI, USA, Oct. 2022, pp. 1–6.
[50] D. G. Holmes and T. A. Lipo, *Pulse Width Modulation for Power Converters: Principle and Practice* (Series on Power Engineering). Hoboken, NJ, USA: Wiley, 2003.
[51] S. Polster, J. Deschler, H. Renner, A. Bocquel, and M. Janssen, "Challenges of large converter-fed synchronous machines for variable-speed pumped hydro storage," *Energies*, vol. 16, no. 22, p. 7506, Nov. 2023.
[52] S. Rahimpour, O. Husev, D. Vinnikov, N. V. Kurdkandi, and H. Tarzamni, "Fault management techniques to enhance the reliability of power electronic converters: An overview," *IEEE Access*, vol. 11, pp. 13432–13446, 2023.

PASCAL M. LINGOM (Student Member, IEEE) received the B.S. and M.S. degrees in pedagogical sciences and electrical engineering from ENSET, University of Douala, Douala, Cameroon, in 2014 and 2016, respectively. He is currently pursuing the Ph.D. degree with the Department of Electrical and Computer Engineering, University of Quebec at Trois-Rivières, QC, Canada. He was a Postgraduate Intern with Opal-RT Technologies, Montreal, Canada, from April 2021 to August 2023, contributing to developing their new courseware in power electronics, motor drives, and renewable energy systems. His current research interests include advanced multilevel power converters for grid-connected renewable energy and variable-speed drive applications and their associated modulation and control techniques.

JOSEPH SONG-MANGUELLE (Senior Member, IEEE) received the B.S. and M.S. degrees in pedagogical sciences and electrical engineering from ENSET, University of Douala, Cameroon, in 1995 and 1997, respectively, and the Ph.D. degree in electrical engineering from the Swiss Federal Institute of Technology, Lausanne, Switzerland, in 2004.

From 2004 to 2012, he held engineering positions with General Electric in Germany, France, and NY, USA, where he was involved in the development of torsional vibration control systems with VFDs and HVDC transmission and distribution systems for future long tieback subsea applications. From 2012 to 2021, he was a Senior Electrical Engineer and a VFD Subject Matter Expert for ExxonMobil, Texas, Russia, and Papua New Guinea, involved in technical qualification of high-power subsea electrical components, facilities design, commissioning, and troubleshooting. From 2021 to 2023, he joined the Oak Ridge National Laboratory, Knoxville, TN, USA, as a Distinguished Research and Development Staff, developing new high-power electronic research programs for the U.S. National Transportation Research Center. He is currently with Shell Corporation as a Global Subject Matter Expert for large variable speed drive systems to accelerate the decarbonization of industry and transportation. In parallel to his professional activities, since 2010, he has been co-supervising master's and Ph.D. students with the University of Douala, Fuzhou University, China, and the University of Quebec at Trois-Rivières, QC, Canada, where is currently an Adjunct Professor. He holds four patents. He is an Associate Editor of the IEEE JOURNAL OF EMERGING AND SELECTED TOPICS IN POWER ELECTRONICS.

SIMON PIERRE BETOKA-ONYAMA (Student Member, IEEE) received the B.S. and M.S. degrees in pedagogical sciences and electrical engineering from ENSET, University of Douala, Douala, Cameroon, in 2012 and 2014, respectively. He is currently pursuing the Ph.D. degree in electrical engineering with the University of Quebec at Trois-Rivières, Trois-Rivières, Canada. His research interests include the analytical evaluation of mechanical stresses in wind turbine systems, electric drives, and power electronics.

MAMADOU LAMINE DOUMBIA (Member, IEEE) received the M.Sc. degree in electrical engineering from Moscow Power Engineering Institute (Technical University), Moscow, Russia, in 1989, the M.Sc. degree in industrial electronics from Université du Québec à Trois-Rivières (UQTR), Trois-Rivières, QC, Canada, in 1994, and the Ph.D. degree in electrical engineering from École Polytechnique de Montreal, Montreal, QC, Canada, in 2000. From 2000 to 2002, he was a Lecturer with École Polytechnique de Montreal and CEGEP Saint-Laurent, Montreal. He was a Senior Research Engineer with the CANMET Energy Technology Centre, Natural Resources Canada, from 2002 to 2003, and a Researcher with the Hydrogen Research Institute (HRI), from 2003 to 2005. Since 2005, he has been a Professor with the Department of Electrical and Computer Engineering, UQTR. He has authored or coauthored more than 100 papers in international journals and conferences. His research interests include renewable energy systems, distributed energy resources, variable speed drives, power electronics, and power quality. He is a member of the IEEE Power Electronics Society and the IEEE Communications Society. He is a Professional Engineer and a member of Ordre des Ingenieurs du Quebec. He is currently an Editorial Board Member of *International Journal of Renewable Energy Research* and *International Journal of Smart Grid.*